JCB Journal of Cell Biology

REPORT

Spindle morphology changes between meiosis and mitosis driven by CK2 regulation of the Ran pathway

Helena Cantwell[1], Hieu Nguyen[2], Arminja N. Kettenbach[2], and Rebecca Heald[1]

The transition from meiotic divisions in the oocyte to embryonic mitoses is a critical step in animal development. Despite negligible changes to cell size and shape, following fertilization the small, barrel-shaped meiotic spindle is replaced by a large zygotic spindle that nucleates abundant astral microtubules at spindle poles. To probe underlying mechanisms, we applied a drug treatment approach using *Ciona* eggs and found that inhibition of casein kinase 2 (CK2) caused a shift from meiotic to mitotic-like spindle morphology with nucleation of robust astral microtubules, an effect reproduced in *Xenopus* egg cytoplasmic extracts. In both species, CK2 activity decreased at fertilization. Phosphoproteomic differences between *Xenopus* meiotic and mitotic extracts that also accompanied CK2 inhibition pointed to RanGTP-regulated factors as potential targets. Interfering with RanGTP-driven microtubule formation suppressed astral microtubule growth caused by CK2 inhibition. These data support a model in which CK2 activity attenuation at fertilization leads to activation of RanGTP-regulated microtubule effectors, inducing mitotic spindle morphology.

Introduction

At the meiosis-to-mitosis transition following fertilization, a rapid shift from reductional meiotic divisions of the oocyte to the first equational mitotic division of the zygote is essential for embryonic development. Though cell size and shape remain similar, the cell division machinery is dramatically reconfigured to facilitate this shift in cell division program (Fig. 1 A). What drives this abrupt change in spindle morphology is an interesting open question.

The spindle is a dynamic, bipolar, microtubule-based structure that in meiosis facilitates the reductional segregation of chromosomes between the oocyte and the much smaller, extruded polar bodies to generate a haploid egg. In mitosis, the spindle faithfully segregates a copy of each chromosome to two daughter cells. Morphometric differences between meiotic and mitotic spindles of early development are well conserved across metazoan species (Crowder et al., 2015). Meiotic spindles are small, barrel-shaped, and anastral across chordates, nematodes, cnidaria, and arthropods and localized close to the cell periphery. In contrast, mitotic spindles are more centrally positioned in the cell and larger, scaling with cell size and displaying arrays of astral microtubules emanating from the spindle poles (Crowder et al., 2015).

Although a gradual change in spindle architecture from meiotic to mitotic divisions was reported in mice (Courtois et al., 2012), a more rapid shift in spindle morphology was observed in other metazoan species, which, unlike rodents but like humans, inherit a centriole from the sperm upon fertilization (Cavazza et al., 2016; Crowder et al., 2015; Schneider et al., 2021). The centriole then recruits cytoplasmic proteins and duplicates to form two centrosomes, which constitute the major microtubule-organizing centers (MTOCs) in mitotic cells. However, the presence of centrioles alone is not sufficient to drive centrosome-mediated astral microtubule nucleation and mitotic spindle morphology. In *Xenopus* egg extracts, spindles formed around sperm chromosomes (with centrosomes) or DNA-coated beads (without centrosomes) both display meiotic anastral morphology, appearing very similar to the meiosis II spindle in unfertilized eggs (Heald et al., 1996). Therefore, cytoplasmic activation of microtubule polymerization pathways likely drives the change in spindle morphology observed at the meiosis-to-mitosis transition.

The main pathways responsible for microtubule growth that contribute to spindle assembly include microtubule nucleation and stabilization around chromatin, nucleation from centrosomes, and branching nucleation from preexisting microtubules. One mechanism stimulating microtubule formation around chromosomes is mediated by the chromosome passenger complex (Maresca et al., 2009), which consists of INCENP, Borealin, Survivin, and Aurora B kinase (Ruchaud et al., 2007; Tseng et al., 2010) and inhibits microtubule depolymerization by

[1]Department of Molecular and Cell Biology, University of California, Berkeley, Berkeley, CA, USA; [2]Department of Biochemistry and Cell Biology, Geisel School of Medicine at Dartmouth College, Hanover, NH, USA.

Correspondence to Helena Cantwell: helena.cantwell@berkeley.edu; Rebecca Heald: bheald@berkeley.edu.

https://doi.org/10.1083/jcb.202407154

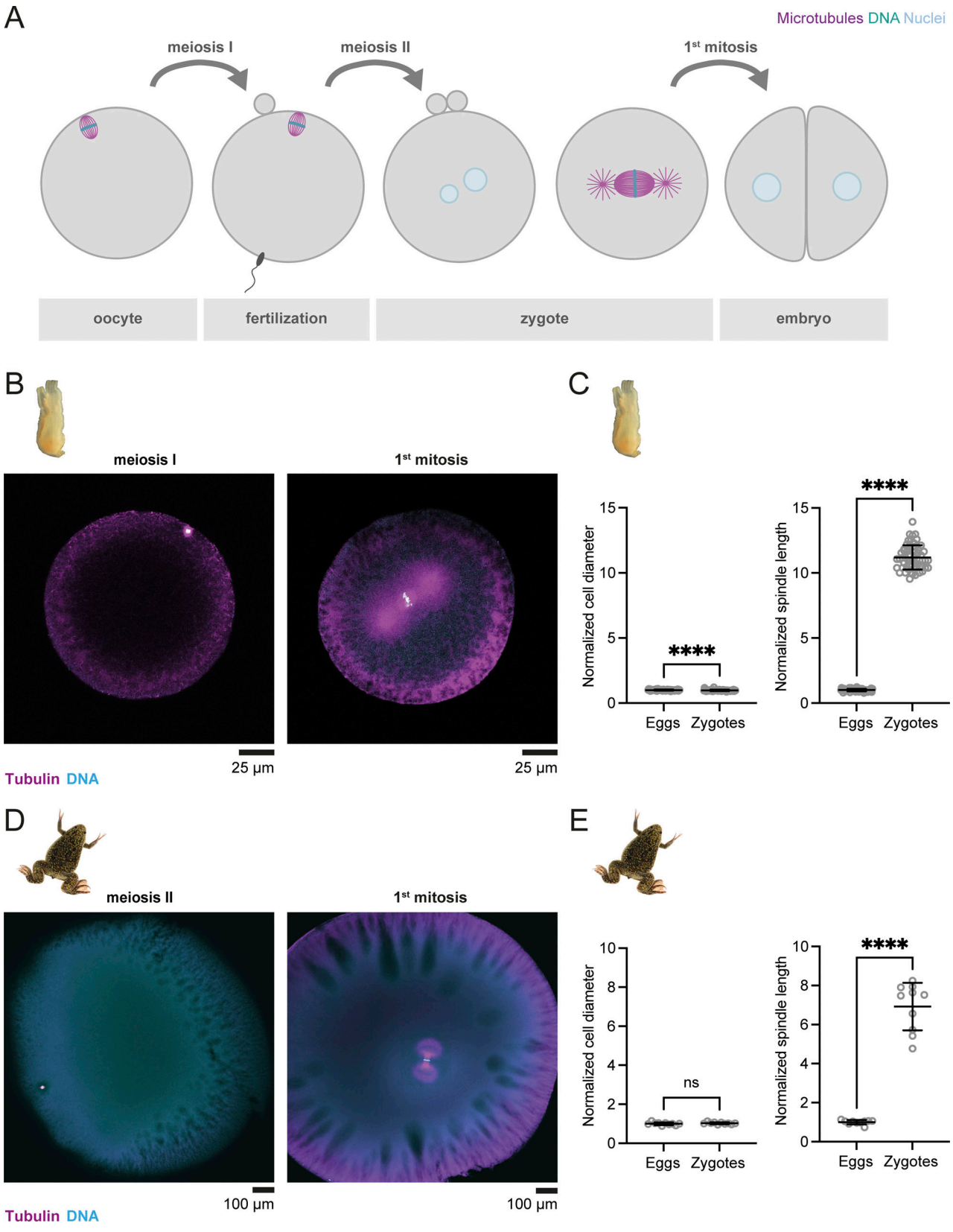

Figure 1. **Spindle morphology changes dramatically between meiosis and mitosis. (A)** Schematic of cellular and spindle morphology changes that accompany the transition from meiotic divisions of the oocyte to the first mitosis of the zygote in early embryogenesis. **(B)** Images of immunofluorescence of a representative *C. robusta* egg in metaphase of meiosis I (left panel) and zygote in metaphase of the first mitosis (right panel). Tubulin (magenta), DNA (cyan). A single z-slice through the center of spindle is shown. **(C)** Normalized *C. robusta* cell diameter (eggs $n = 58$, zygotes $n = 58$) and metaphase spindle length (eggs $n = 58$, zygotes $n = 58$) in meiosis and mitosis. Measurements are normalized to average egg cell diameter or pole-to-pole spindle length. The line indicates the

mean, and the error bars indicate one standard deviation above and below the mean. **(D)** Images of immunofluorescence of a representative *X. laevis* egg in metaphase of meiosis II (left panel) and zygote in metaphase of the first mitosis (right panel). Tubulin (magenta), DNA (cyan). Maximum intensity projection is shown. **(E)** Normalized *X. laevis* cell diameter (eggs n = 10, zygotes n = 10) and metaphase spindle length (eggs n = 10, zygotes n = 10) in meiosis and mitosis. Measurements are normalized to average egg cell diameter or spindle length. The line indicates the mean, and the error bars indicate one standard deviation above and below the mean. Statistical significance was determined by two-tailed Mann–Whitney tests (ns = not significant, **** = $P < 0.00005$).

MCAK (Sampath et al., 2004) and stathmin (Gadea and Ruderman, 2006; Kelly et al., 2007), contributing to spindle microtubule stability. A second major pathway of microtubule nucleation and organization around chromosomes is driven by RanGTP, which is generated by its chromatin-bound guanine nucleotide exchange factor RCC1 (Kalab et al., 2002; Oh et al., 2016). A RanGTP gradient leads to localized release of spindle assembly factors (SAFs) from the transport receptors importin α and importin β that sequester them in the cytoplasm by binding to their nuclear localization signal (NLS) sequences (Carazo-Salas et al., 1999; Kalab et al., 1999; Kalab et al., 2002; Nachury et al., 2001; Ohba et al., 1999; Wiese et al., 2001; Wilde and Zheng, 1999). A number of importin-regulated SAFs with roles in spindle microtubule nucleation and organization have been identified (Cavazza and Vernos, 2016), including TPX2 (Gruss et al., 2001; Scrofani et al., 2015), XCTK2 (Ems-McClung et al., 2020, 2004), NuMA (Nachury et al., 2001), and augmin (Ustinova et al., 2023). Partitioning of importin α between the plasma membrane and cytoplasm is a mechanism by which NLS-containing cargoes are regulated to promote scaling of spindle size with decreasing cell size during development (Brownlee and Heald, 2019; Rieckhoff et al., 2020).

Another major spindle assembly pathway, active in mitotic cells, is mediated by microtubule nucleation at centrosomes. The centrosome, a pair of centrioles surrounded by pericentriolar material, concentrates gamma-tubulin ring complexes (γ-TURCs), leading to microtubule nucleation and stabilization (Helmke et al., 2013; Wu and Akhmanova, 2017). Meiotic oocytes lack functional centrosomes but retain centrosomal proteins (Peshkin et al., 2019; Wang et al., 2016), some of which have been shown to function with pericentriolar material components and γ-TURC to nucleate microtubules at acentriolar MTOCs (So et al., 2019). In mouse oocytes, a liquid-like domain at spindle poles concentrates regulatory factors promoting spindle assembly (So et al., 2019). Microtubules can also be nucleated on preexisting microtubules; branching microtubule nucleation mediated by the RanGTP-regulated SAFs augmin and TPX2 contributes to spindle assembly (Petry et al., 2013; Ustinova et al., 2023; Wu and Akhmanova, 2017). Microtubule plus end–binding proteins such as EB3/CLIP-170 and XMAP215/TOG concentrate tubulin and stimulate microtubule polymerization, contributing to this and other nucleation pathways (Kraus et al., 2023; Miesch et al., 2023; Thawani et al., 2018).

How these microtubule nucleation and stabilization pathways are integrated to facilitate formation of the specialized meiotic spindle and, just one cell cycle later, the mitotic spindle of the zygote remains mysterious. In a study of spindle morphology across a wide range of species, the most dramatic shift in morphology observed at the meiosis-to-mitosis transition was in the sea squirt *Ciona robusta* (Crowder et al., 2015), a simple chordate species that is the closest living relative of vertebrates (Christiaen et al., 2009a). We exploit this robust change in spindle morphology to screen for small molecule inhibitors that perturb it. We then take advantage of the biochemical tractability of *Xenopus laevis* egg and embryo extracts capable of recapitulating meiotic and mitotic spindle assembly (Maresca and Heald, 2006; Wilbur and Heald, 2013) to probe candidate pathways and mechanisms. We propose that a decrease in casein kinase 2 (CK2) activity following fertilization leads to activation of the RanGTP pathway of microtubule polymerization at spindle poles, thereby contributing to astral microtubule growth and mitotic spindle morphology.

Results and discussion

Spindle morphology changes dramatically between meiosis and mitosis in both *C. robusta* and *X. laevis*

To characterize the spindle morphology changes that accompany the meiosis-to-mitosis transition in chordates (Fig. 1 A), we visualized microtubules and DNA by immunofluorescence in fixed eggs and zygotes of *C. robusta* and *X. laevis*. *C. robusta* eggs and sperm were isolated from hermaphrodite adults, and in vitro fertilization was carried out to generate populations of synchronously dividing embryos. *C. robusta* eggs are arrested in metaphase of meiosis I and display a small, barrel-shaped anastral spindle, ∼10.5 µm in length, close to the cell periphery (Fig. 1 B and Fig. S1 A). Though the overall cell size and shape of the zygote are similar to that of the egg (Fig. 1, B and C; and Fig. S1 A), the first mitotic spindle in metaphase is ∼11-fold longer than its meiotic counterpart, more centrally positioned in the cell, and displays large arrays of astral microtubules emanating from the spindle poles (Fig. 1, B and C; and Fig. S1 A); these microtubule arrays extend toward the cell cortex in anaphase (Fig. S1 B). *X. laevis* in vitro fertilization was carried out to generate synchronously dividing populations of zygotes. *X. laevis* eggs are much larger (∼1.4-mm diameter) than *C. robusta* eggs (∼150-µm diameter) (Fig. S1, A and C) and arrested in metaphase of meiosis II. Like those of *C. robusta*, *X. laevis* egg meiotic spindles are small (∼26 µm in length), barrel-shaped, anastral, and localized in close proximity to the egg periphery, whereas zygotic mitotic spindles are ∼6.9-fold longer, have astral microtubules arrays at the poles, and are more centrally positioned in the cell (Fig. 1, D and E; and Fig. S1, C and D).

CK2 inhibition stimulates astral microtubule assembly, and CK2 activity decreases at fertilization in both *Ciona* and *Xenopus*

To identify upstream pathways underlying the conserved, abrupt change in spindle morphology that occurs following fertilization, we carried out a small set of drug treatments to

identify inhibitors that perturb meiotic spindle morphology in *C. robusta*. We focused on targets previously reported or hypothesized to modulate known spindle assembly pathways, then examined spindle morphology by immunofluorescence. In contrast to treatment with the other drugs (Fig. S2 A), treatment with silmitasertib (CK2i), a CK2 inhibitor, led to a dramatic change in meiotic spindle morphology, pushing it toward a more mitotic-like architecture (Fig. 2 A). A 1-h treatment with CK2i caused the majority of oocytes (78%) to form spindles with dramatic arrays of astral-like microtubules emanating from the poles and ectopic sites of microtubule nucleation in close proximity to the spindle, with a further 20% displaying a similar but milder phenotype (Fig. 2 B). The number of foci of microtubule nucleation in a network around the spindle increased upon CK2i treatment (Fig. 2 C).

We next assessed the effects of CK2 inhibition on meiotic spindle morphology in *Xenopus* egg extracts (Maresca and Heald, 2006) (Fig. 2 D). In contrast to the anastral, barrel-shaped spindles formed around *Xenopus* sperm chromosomes in control reactions, CK2i treatment shifted spindle architecture toward a more mitotic-like morphology, with astral-like microtubules emanating from the poles (Fig. 2, D and E), increased spindle length (Fig. 2 F), increased tubulin intensity at spindle poles (Fig. 2 G and Fig. S2 B), and an increased frequency of ectopic microtubule asters in close proximity to the spindle (Fig. S2 C). Inhibition of CK2 with a second inhibitor, 4,5,6,7-tetrabromobenzotriazole (TBB), had a similar effect on meiotic spindle morphology in extracts, increasing the frequency of spindles with astral-like microtubules emanating from the poles (Fig. S2, D and E), and partial immunodepletion of CK2α from egg extracts led to increased half spindle length with astral-like microtubules at the poles (Fig. S2, F–H). Therefore, multiple methods of inhibiting CK2 in meiotic *Xenopus* cytoplasmic extracts recapitulate the effects of CK2 inhibition observed in *C. robusta* oocytes, indicating that CK2 regulation of spindle microtubule organization is conserved across chordates.

If attenuation of CK2 activity plays a physiological role in the alteration of spindle morphology observed following fertilization, then its kinase activity is predicted to decrease between metaphase of meiosis II and metaphase of the first mitosis. Utilizing a commercial CK2 activity assay with a model substrate, we measured CK2 activity in cell lysates of eggs in metaphase of meiosis II and zygotes in metaphase of the first mitosis of both *C. robusta* and *X. laevis*. In both species, CK2 activity decreased between metaphase of the final meiotic and first mitotic division (Fig. 2, H and I). In *Ciona*, this drop in activity is likely caused by degradation of regulatory subunit CK2β (Russo et al., 2004), while mechanisms regulating CK2 activity in *Xenopus* remain unclear. To assess the effects of CK2 inhibition on mitotic spindles, we inhibited CK2 in metaphase-arrested mitotic embryo extracts prepared from stage 8 embryos (Wilbur and Heald, 2013) and observed few changes to spindle morphology with a very modest decrease in spindle length, no significant change in tubulin intensity at spindle poles, and a similar distribution of spindle morphologies to that of the untreated control (Fig. S2, I–L). The observations that CK2 activity decreases at fertilization and that its inhibition in meiosis leads to mitotic-like spindle morphology made CK2 a strong candidate to be an upstream regulator of spindle architecture during development.

Minor CK2-regulated changes to the metaphase proteome accompany the meiosis-to-mitosis transition

CK2 phosphorylates hundreds of different substrates implicated in many signaling pathways and biological processes (Borgo et al., 2021; Meggio and Pinna, 2003). We reasoned that either direct substrates of CK2 or proteins in downstream pathways could regulate spindle morphology. To identify potential candidates at the level of the proteome, we first cataloged changes in protein abundance between meiosis and mitosis then compared them to those observed upon CK2 inhibition.

To assess overall changes in protein composition between meiosis and mitosis, we carried out spindle assembly reactions in metaphase-arrested meiotic egg or metaphase-arrested mitotic stage 8 embryo extracts and compared their proteomes by tandem mass tag (TMT) analysis (Fig. 3 A). To increase coverage, we carried out this analysis twice, resulting in two datasets (dataset 1 and dataset 2), each containing three biological replicates.

At the proteome level (Table S1), 13,448 proteins were detected (11,686 in dataset 1 and 10,874 in dataset 2, with 9,112 (68%) overlapping). Of these, 238 were enriched in meiosis compared to mitosis (Fig. 3 B and Fig. S4), including Mos, which is degraded upon fertilization (Nishizawa et al., 1993), and ovochymase, which is secreted upon egg activation (Lindsay et al., 1999). 662 proteins were enriched in mitosis compared to meiosis (Fig. 3 B and Fig. S4). Interestingly, gene ontology (GO) analysis of proteins overrepresented in meiosis relative to mitosis (Table S3) revealed 6 microtubule-binding proteins (Table S4), including gamma-tubulin complex component 4, a component of the γ-TURC (Oakley et al., 2015). GO categories overrepresented in mitosis relative to meiosis were mostly terms related to cellular membranes and membrane-bound organelles, including the endoplasmic reticulum and Golgi apparatus (Table S5).

To determine whether any proteins changing level between meiosis and mitosis were regulated by CK2, we compared the proteome of meiotic and mitotic cytoplasmic extracts upon addition of DMSO control or CK2i at a concentration confirmed by kinase assay to reduce CK2 activity (Fig. S3, A–C) but that did not perturb the metaphase arrest of the extract as determined by fluorescence microscopy (Table S1, Fig. S2 I, and Fig. S3 D). Relatively minor changes were seen in the total proteome upon drug treatment (Fig. 4, A and B; and Fig. S4), with 59 candidate proteins changing level significantly between meiosis and mitosis and in the same direction upon CK2 inhibition (Fig. 4, C and D). However, none of these proteins have known roles in microtubule binding or cell division, and the only statistically enriched GO category was T cell receptor signaling.

Altogether, this analysis reveals some interesting differences between meiotic and mitotic proteomes that may contribute to the change in cell division program. However, since changes in protein levels upon CK2 inhibition were minor, such protein abundance regulation is unlikely to directly underlie CK2

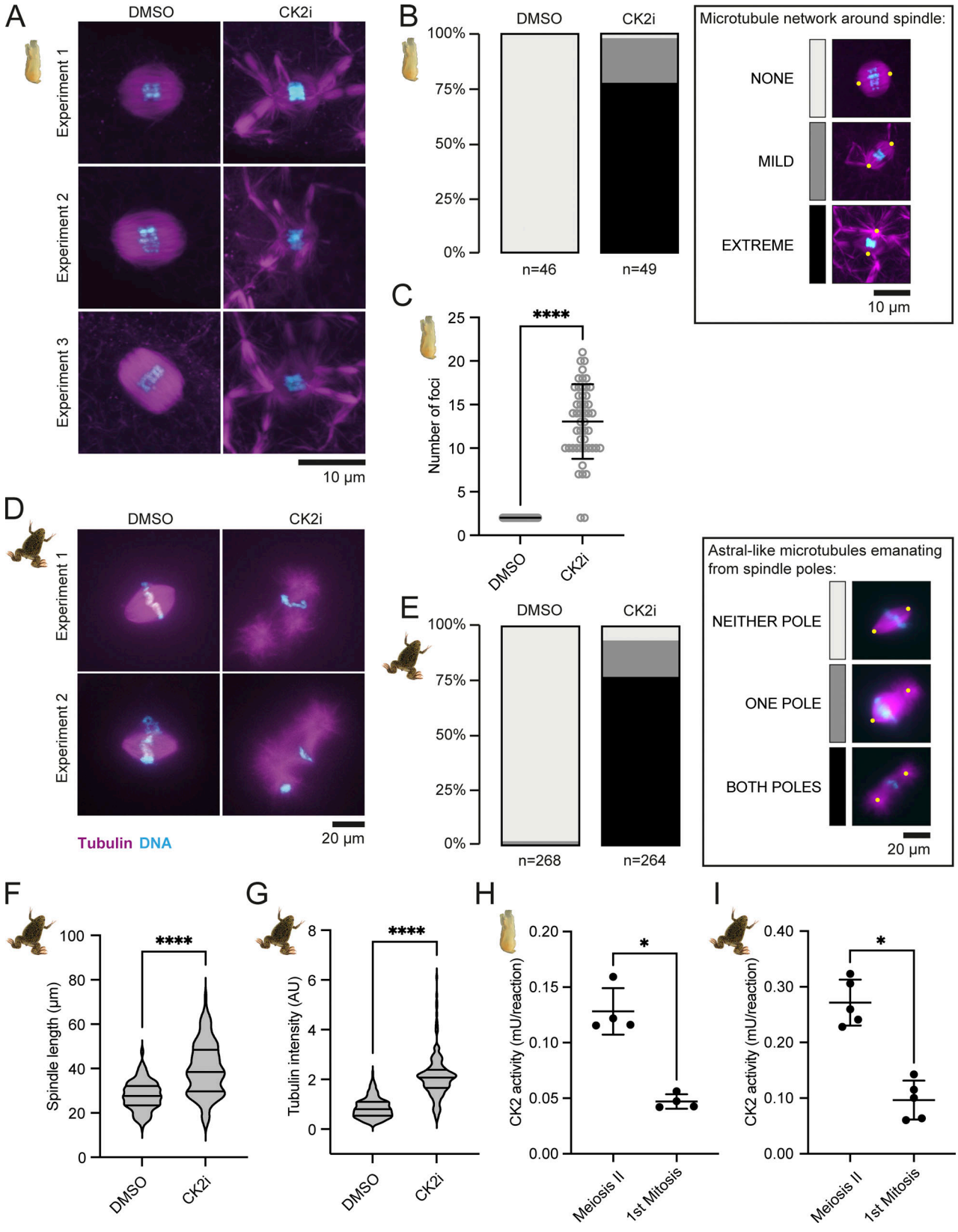

Figure 2. **Inhibition of CK2 alters meiotic spindle morphology, and CK2 activity decreases between meiosis and mitosis. (A)** Images of immunofluorescence of representative *C. robusta* oocytes treated for 1 h with DMSO or 250 µM silmitasertib (CK2i) as indicated for three independent experimental replicates. Maximum intensity projections are shown. Tubulin (magenta), DNA (cyan). Experiment 2 DMSO control spindle image is the same as DMSO control spindle image in Fig. S2 A. Experiment 3 DMSO control spindle is image of the same spindle shown as DMSO control spindle in Fig. 5 A. **(B)** % of *C. robusta* oocytes displaying no (NONE), a limited (MILD), or an extensive (EXTREME) microtubule network around the spindle following treatment for 1 h with DMSO or 250 µM

CK2i as indicated. Results from five independent experiments were pooled (n = 46 oocytes [DMSO], n = 49 oocytes [CK2i]). Representative image of each analysis category is shown with spindle poles indicated by yellow dots. Representative images of each analysis category shown are the same as representative images of each analysis category shown in Fig. 5 B. Representative image of EXTREME analysis category is used as representative CK2i spindle image in Fig. 5 A. **(C)** Number of foci of microtubule nucleation in 529-μm^2 area around metaphase plate DNA in *Ciona* oocytes treated for 1 h with 250 µM CK2i or DMSO as indicated. Results from five independent experiments were pooled (n = 36 oocytes [DMSO], n = 49 oocytes [CK2i]). The line indicates the mean, and the error bars indicate one standard deviation above and below the mean. Statistical significance was determined by a two-tailed Mann–Whitney test (**** = P < 0.0001). **(D)** Images of immunofluorescence of representative spindles formed in metaphasic CSF *X. laevis* egg extract in the presence of 50 µM CK2i or DMSO as indicated for two independent experimental replicates. Maximum intensity projections are shown. Tubulin (magenta), DNA (cyan). **(E)** Percentage of bipolar spindles displaying astral-like microtubules emanating from both poles, one pole, or neither pole in metaphasic CSF *X. laevis* egg extract in the presence of 50 µM CK2i or DMSO as indicated. Data from four independent extract experiments were pooled (n = 264 spindles [CK2i], n = 268 spindles [DMSO]); $n \geq 40$ spindles per condition for each extract. Representative image of each analysis category is shown with spindle poles indicated by yellow dots. **(F)** Violin plot of spindle length of spindles from spindle assembly reactions carried out in *Xenopus* egg extract in the presence of DMSO or 50 µM CK2i as indicated. $n \geq 136$ spindles per condition (from three cytoplasmic extracts [$n \geq 25$ per condition per extract]). Statistical significance was determined by a two-tailed Mann–Whitney test (**** = P < 0.0001). For violin plots, lines indicate median and upper and lower quartiles. **(G)** Violin plot of β-tubulin intensity at spindle pole of spindles from spindle assembly reactions carried out in *Xenopus* egg extract in the presence of DMSO or 50 µM CK2i as indicated. $n \geq 210$ spindle poles per condition (from three cytoplasmic extracts [$n \geq 42$ per extract]). Tubulin intensity normalized to mean of DMSO control. Statistical significance was determined by a two-tailed Mann–Whitney test (**** = P < 0.0001). **(H and I)** CK2 activity (mU/reaction) of cell lysates of meiosis II metaphase and first mitotic metaphase *C. robusta* (H) (n = 4 lysates) and *X. laevis* (I) (n = 5 lysates) eggs and embryos, respectively. Statistical significance was determined by two-tailed Mann–Whitney tests (* = P < 0.05). The line indicates the mean, and the error bars indicate one standard deviation above and below the mean.

activity–mediated differences between meiotic and mitotic spindle morphology.

Phosphoproteomics in CK2-inhibited *Xenopus* cytoplasmic extracts identifies candidate phosphoregulated proteins and downstream pathways

Given the rapid shift in spindle microtubule organization at the meiosis-to-mitosis transition, we reasoned that changes in posttranslational modifications, particularly phosphorylation, were likely to drive the transition (Peuchen et al., 2017). We assessed the global phosphoproteome and detected 37,339 phosphopeptides (Table S2). 2,298 of these were enriched in meiotic and 5,673 in mitotic extracts, corresponding to a total of 1,478 and 1,584 proteins, respectively (Fig. 3 C and Fig. S5). Whereas GO analysis did not reveal specific categories of proteins with meiosis-enriched phosphosites, 89 spindle-localized proteins were identified with phosphosites enriched in mitosis (Tables S6 and S7), including TPX2, HAUS augmin-like complex components HAUS5, HAUS6, and HAUS8, TACC3, and kinases Polo 1 kinase and cyclin-dependent kinase 1. We next assessed the effect of CK2 inhibition on the phosphoproteome (Fig. 4, E and F; and Fig. S5). 53 phosphopeptides from 43 proteins changed in level in the same direction both between meiotic and mitotic extracts and upon CK2i addition to meiotic extract (Fig. 4, G and H). Phase normalization (see Materials and methods) to account for higher total phosphorylation levels in mitotic extract identified a further 35 candidate proteins that change at the phosphopeptide but not the protein level, making them candidates for phosphoregulated proteins that drive the change in spindle morphology.

Of the 78 candidate proteins identified by this approach, 38 were previously reported to be associated with the vertebrate spindle or RanGTP-stabilized microtubules by proteomic analyses (Rao et al., 2016; Rosas-Salvans et al., 2018) or by localization to spindles, centrosomes, or kinetochores (Huang et al., 2015) (Table S8). Network analysis using the STRING database (Szklarczyk et al., 2019) revealed functional clusters of these phosphoregulated proteins with reported roles in DNA replication, nucleocytoplasmic transport, splicing, translation, microtubule binding, chromatin modification, transcription regulation, chromosome condensation, DNA repair, and tight junction assembly (Fig. 4 I). Recent work has demonstrated noncanonical roles in cell cycle control for many proteins, notably nucleocytoplasmic transport proteins in spindle assembly (Yang et al., 2023), and our candidates included two proteins reported to be Ran-regulated: nucleoporin NUP214 (Askjaer et al., 1999; Hutten and Kehlenbach, 2006) and cell cycle regulator geminin (Blow, 2003; Hodgson et al., 2002). Based on literature searches, we hypothesize that a further five candidates are likely also Ran-regulated: nucleocytoplasmic transport proteins NUP35 and AKIRIN2 (De Almeida et al., 2021), transcription regulator CTR9 homolog (Kimura et al., 2017; Taltynov et al., 2013), DNA helicase MCM4 (Yamaguchi and Newport, 2003), and telomere-associated protein RIF1 (Sukackaite et al., 2017). Thus, a subset of candidate proteins downstream of CK2 are regulated by RanGTP.

Overall, our phosphoproteomic analysis reveals numerous interesting differences between phosphorylation patterns in meiosis and mitosis and points to Ran-regulated proteins as potential targets of CK2 regulation that differ between these two distinct cell division programs. This intrigued us, as inhibition of CK2 resulted in the formation of astral microtubule networks that mimic previously reported effects of adding constitutively active RanGTP to meiotic *Xenopus* egg extract. Addition of Ran^{G19V} to spindle assembly reactions led to the formation of abundant MTOCs, mostly not directly associated with chromatin, and when no chromatin source was added microtubule networks, similar to those we observe around the spindles in *Ciona* oocytes following CK2 inhibition, formed (Kalab et al., 1999).

Inhibition of the RanGTP spindle assembly pathway suppresses effects of CK2 inhibition

To test whether the effect of CK2 inhibition on spindle morphology was mediated by the RanGTP pathway, we used the drug importazole, which inhibits the interaction between RanGTP and importin-β (Soderholm et al., 2011). Strikingly, treatment of *C. robusta* oocytes with importazole suppressed

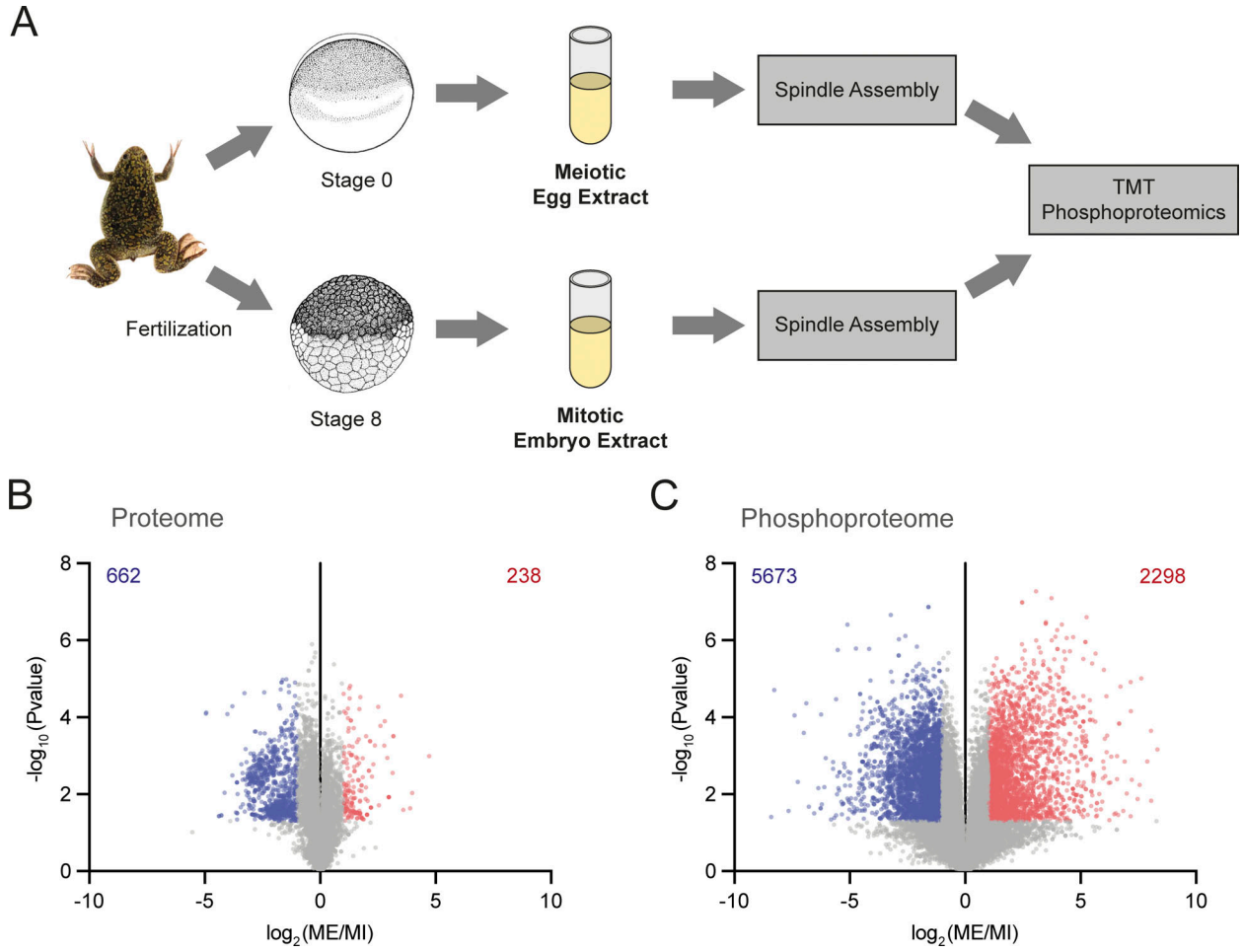

Figure 3. **Proteomic and phosphoproteomic changes between meiosis and mitosis. (A)** Schematic of phosphoproteomics experimental setup. *Xenopus* illustrations © Natalya Zahn (2022) (Fisher et al., 2023; Zahn et al., 2022). **(B)** Volcano plot of $\log_2$ ratio (protein abundance) versus $-\log_{10}$ P value for individual proteins in meiosis compared to mitosis (ME/MI). Red points indicate significantly enriched ($\log_2$ ratio >1 and P value <0.05) proteins (total number indicated in red). Blue points indicate significantly depleted ($\log_2$ ratio less than −1 and P value <0.05) proteins (total number indicated in blue). *n* = 16,105 proteins. **(C)** Volcano plot of $\log_2$ ratio (phosphopeptide abundance) versus $-\log_{10}$ P value for individual phosphopeptides in meiosis compared to mitosis (ME/MI). Red points indicate significantly enriched ($\log_2$ ratio >1 and P value <0.05) phosphopeptides (total number indicated in red). Blue points indicate significantly depleted (ratio $\log_2$ less than −1 and P value <0.05) phosphopeptides (total number indicated in blue). *n* = 28,612 phosphopeptides. Datasets 1 and 2 were combined and visualized together in this figure. Individual datasets are visualized separately in Fig. S4 (proteome) and Fig. S5 (phosphoproteome).

the effects of CK2 inhibition on spindle morphology (Fig. 5 A), reducing the frequency of oocytes with spindles showing extreme defects with dramatic arrays of astral-like microtubules emanating from the poles upon CK2i treatment from 70% to 3%; when treated with both drugs, 51% of spindles displayed no astral-like microtubules emanating from the poles or ectopic sites of microtubule nucleation in close proximity to the spindle, and 46% displayed mild defects, with a small number of microtubule bundles emanating from the poles (Fig. 5 B).

Consistent with a role for RanGTP in mediating the effects of CK2 inhibition, importazole treatment also suppressed the effects of CK2 inhibition on spindle formation when added to *Xenopus* egg extracts. To minimize the effects of redundant mechanisms that drive spindle assembly, we examined microtubule arrays 30 min after initiating spindle assembly reactions, when half spindles with a single pole had formed. Half spindles formed in the presence of CK2i displayed increased length with large asters at the half spindle poles; importazole treatment suppressed this length increase, reducing the size of the aster at the pole (Fig. 5, C and E). The increased β-tubulin intensity at the spindle pole observed upon CK2 inhibition was also suppressed by importazole treatment (Fig. 5 F). Addition of importin-β(71–876) protein, a truncated mutant unable to bind to RanGTP that sequesters cargoes (Nachury et al., 2001), also suppressed the effects of CK2 inhibition on half spindle length and tubulin intensity at the poles (Fig. 5, D, H, and I).

We hypothesized that the effects of CK2 inhibition on spindle assembly are likely mediated by increased recruitment of importin-β SAF cargoes to spindle poles. To assess this, we monitored the localization of the SAF TPX2, an importin-β cargo implicated in microtubule nucleation that localizes strongly to spindle poles in control reactions (Fig. S6 A). Intensity of both TPX2 and tubulin at the poles was reduced upon addition of importazole or importin-β(71–876) (Fig. S6). Both treatments suppressed the

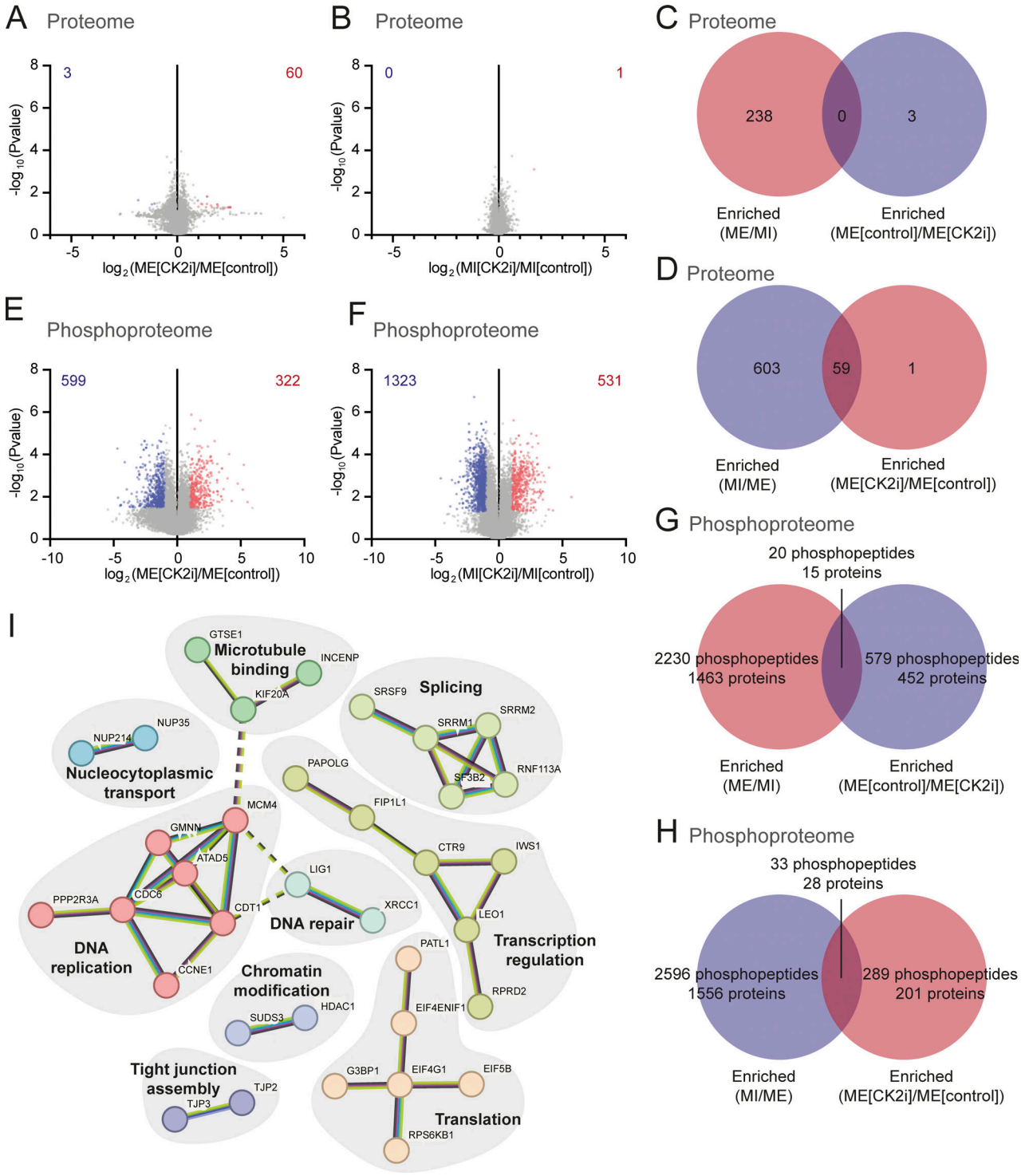

Figure 4. **Proteomic and phosphoproteomic changes upon CK2 inhibition. (A and B)** Volcano plots of $\log_2$ ratio (protein abundance) versus $-\log_{10}$ P value for individual proteins in meiosis in the presence of CK2 inhibitor (CK2i) compared to meiosis in the absence of CK2i (A) and mitosis in the presence of CK2i compared to mitosis in the absence of CK2i (B), respectively. Red points indicate significantly enriched ($\log_2$ ratio >1 and P value <0.05) proteins (total number indicated in red). Blue points indicate significantly depleted ($\log_2$ ratio less than −1 and P value <0.05) proteins (total number indicated in blue). *n* = 16,105 proteins. **(C)** Venn diagram indicating the number of unique proteins in the categories enriched in meiosis relative to mitosis and enriched in meiosis in the absence of CK2i relative to meiosis in the presence of CK2i and in the overlap between these two categories. **(D)** Venn diagram indicating the number of unique proteins in the categories enriched in mitosis relative to meiosis and enriched in meiosis in the presence of CK2i relative to meiosis in the absence of CK2i and in the overlap between these two categories. **(E and F)** Volcano plots of $\log_2$ ratio (phosphopeptide abundance) versus $-\log_{10}$ P value for individual phosphopeptides in meiosis in the presence of CK2i compared to meiosis in the absence of CK2i (*n* = 28,583 phosphopeptides) (E) and mitosis in the presence of CK2i compared to mitosis in the absence of CK2i (*n* = 28,597 phosphopeptides) (F), respectively. Red points indicate significantly enriched ($\log_2$ ratio >1 and P value <0.05) phosphopeptides (total number indicated in red). Blue points indicate significantly depleted ($\log_2$ ratio less than −1 and P value <0.05)

phosphopeptides (total number indicated in blue). **(G)** Venn diagram indicating the number of unique phosphopeptides and proteins containing phosphopeptides in the categories enriched in meiosis relative to mitosis and enriched in meiosis in the absence of CK2i relative to meiosis in the presence of CK2i and in the overlap between these two categories that do not exhibit protein-level changes in the same directions. **(H)** Venn diagram indicating the number of unique phosphopepetides and proteins containing phosphopeptides in the categories enriched in mitosis relative to meiosis and enriched in meiosis in the presence of CK2i relative to meiosis in the absence of CK2i and in the overlap between these two categories that do not exhibit protein-level changes in the same directions. **(I)** STRING network analysis of candidate proteins carried out using full STRING network annotations with high confidence (interaction score ≥0.7). Edge color indicates data source with known interactions shown in cyan (from curated databases) and magenta (experimentally determined), predicted interactions shown in emerald green (gene neighborhood), red (gene fusions), royal blue (gene co-occurrence), lime green (text mining), black (co-expression), and lilac (protein homology). K-means clustering with default parameters was used to define functional clusters. The dashed lines represent edges between clusters. CK2i was added at a concentration of 25 µM in meiotic extract and 10 µM in mitotic extract. Datasets 1 and 2 were combined and visualized together in this figure. Individual datasets are visualized separately in Fig. S4 (proteome) and Fig. S5 (phosphoproteome).

increase in TPX2 intensity at the poles observed upon CK2 inhibition (Fig. 5, C, D, G, and J). These results support a model in which a decrease in CK2 kinase activity following fertilization modulates activity of a number of RanGTP-regulated importin cargoes, including TPX2, increasing microtubule nucleation and polymerization at spindle poles (Fig. 5 K) and contributing to the difference between meiotic and mitotic spindle morphology.

Our results suggest a global effect on the RanGTP pathway at the meiosis-to-mitosis transition that stimulates localization of SAFs at spindle poles and astral microtubule formation. One possible explanation is that CK2-mediated phosphorylation inhibits RanGAP, its GTPase-activating protein that forms a complex with Ran and RanBP1 and promotes the hydrolysis of RanGTP to RanGDP. CK2 phosphorylation of RanGAP1 on serine 358, a site conserved in *Xenopus*, increases the efficiency of RanGAP1–Ran–RanBP1 complex formation in humans, which could affect RanGTP hydrolysis rate and the spatial activation of SAFs (Caudron et al., 2005; Gruss and Vernos, 2004; Kalab and Heald, 2008; Takeda et al., 2005). Partitioning of importin α between cellular membranes and the cytoplasm, where it binds and inhibits SAFs, is also regulated by CK2-mediated phosphorylation (Brownlee and Heald, 2019; Hachet et al., 2004). Unfortunately, these phosphosites on RanGAP and importin α were not present in our phosphoproteomic dataset, and further work will be needed to investigate their regulation by CK2 at the meiosis-to-mitosis transition.

The RanGTP pathway has previously been implicated in meiotic spindle assembly in multiple systems (Cavazza and Vernos, 2016; Cesario and McKim, 2011; Drutovic et al., 2020; Dumont et al., 2007; Gruss et al., 2001). Our data indicate that this pathway, differentially regulated, is also important for determining mitotic spindle morphology in early embryos. This supports the conclusions of recent work that demonstrated that the RanGTP pathway is essential for mitotic spindle assembly during very early embryonic divisions of medaka fish embryos (Kiyomitsu et al., 2024) and work showing that spindle assembly in *X. laevis* early embryo cytoplasmic extracts (stage 3) was dependent on the RanGTP pathway (Wilbur and Heald, 2013).

The meiosis-to-mitosis transition and embryonic viability

The first mitotic division of human embryos is frequently error prone (Cavazza et al., 2021; Currie et al., 2022), contributing to the high rates of aneuploidy in early embryos (Coticchio et al., 2023; Lee and Kiessling, 2017). Very little is known about what regulates the spindle morphology change at the shift from egg to zygote, a process critical for accurate chromosome segregation in the first mitosis. Our study implicates CK2 and the RanGTP pathway in the regulation of this spindle morphology transition in both frogs and sea squirts, suggesting likely conservation of regulatory mechanisms across species. Overexpression of HSET (kinesin-14) in mouse oocytes elongated spindles, making them more mitotic-like (Bennabi et al., 2018), and expression of mutant INCENP in *Drosophila* oocytes led to ectopic aster formation in proximity to the spindle (Colombié et al., 2008), suggesting these factors may also contribute to the spindle morphology change. A recent preprint demonstrated that inhibition of the Mos–MAPK pathway led to a shift in spindle morphology to mitotic-like in starfish oocytes (Avilov et al., 2023, *Preprint*), suggesting this signaling pathway, which is active in meiosis but inactivated at fertilization (Dupré et al., 2011), may be part of the upstream control.

Here we have focused on spindle morphology but our global phosphoproteomic approach also provides a dataset in which we can probe changes in the regulation of other cellular processes that accompany the meiosis-to-mitosis transition. Changes to chromosome condensation (Bomar et al., 2002) and cohesion (Tachibana-Konwalski et al., 2010), cell cycle regulation (Kubiak et al., 2008), and centrosome regulation (Manandhar et al., 2005) accompany the transition from egg to zygote. Interestingly, proteins with phosphosites enriched in mitosis compared to meiosis in our dataset included condensins, NUSAP1, histones H1.3 and H1.8, and 74 centrosomal proteins, suggesting phosphoregulation of chromosome condensation and centrosome regulation between meiosis and mitosis. Future work will explore the molecular basis of these changes and the contribution of phosphoregulation to ensuring they are brought about accurately at the appropriate time in development to ensure embryonic viability.

Materials and methods

Ciona husbandry, gamete collection, and in vitro fertilization

C. robusta adult animals were obtained from M-Rep and maintained at 16°C in artificial seawater (Instant Ocean). Gametes were obtained by dissection of egg ducts and sperm ducts from gravid animals (Christiaen et al., 2009b). Eggs and sperm from 6 to 12 animals were mixed for each experiment. For in vitro fertilizations, sperm was activated by mixing with basic artificial seawater (10 µl 1 M Tris [pH 9/10], in 6 ml seawater) in a

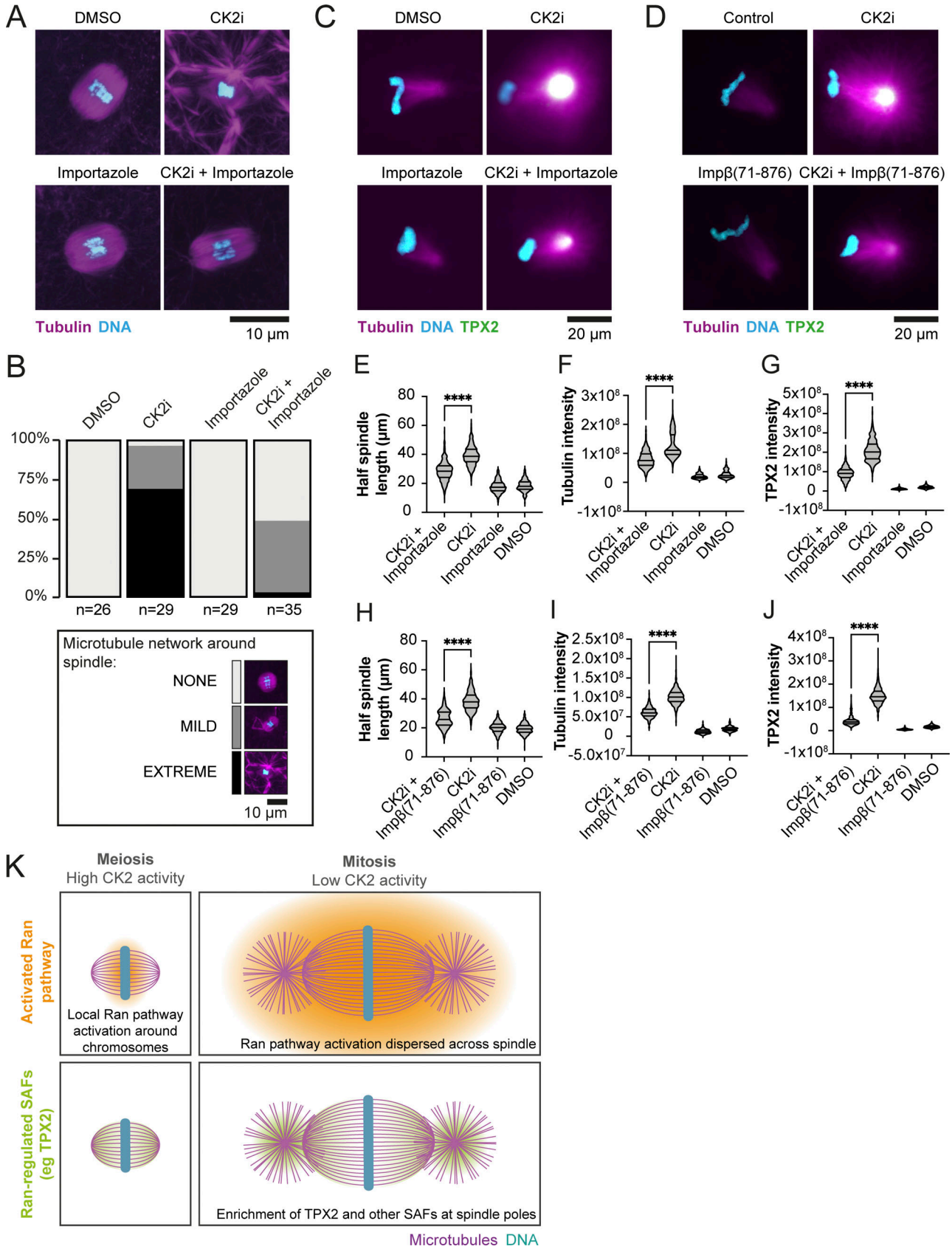

Figure 5. **Inhibition of RanGTP-mediated spindle assembly pathway suppresses effects of CK2 inhibition in *C. robusta* eggs and *X. laevis* egg extracts.** **(A)** Images of immunofluorescence of representative *C. robusta* oocytes treated for 1 h with DMSO, 250 µM CK2i, 250 µM importazole or 250 µM CK2i and 250 µM importazole, as indicated. Maximum intensity projections are shown. Tubulin (magenta), DNA (cyan). DMSO control spindle is image of the same spindle

shown as experiment 3 DMSO control spindle in Fig. 2 A. CK2i spindle image is used as a representative image of EXTREME analysis category in Fig. 2 B and Fig. 5 B. **(B)** % of *C. robusta* oocytes displaying no (NONE), a limited (MILD), or an extensive (EXTREME) microtubule network around the spindle following treatment for 1 h with DMSO, 250 µM CK2i, 250 µM importazole or 250 µM CK2i and 250 µM importazole as indicated. Results from three independent experiments were pooled (n = 26 oocytes [DMSO], n = 29 oocytes [CK2i], n = 29 oocytes [importazole], n = 35 oocytes [CK2i + importazole]). Data shown for DMSO and CK2i are a subset of that shown in Fig. 2 B. Representative images of each analysis category shown are the same as representative images of each analysis category shown in Fig. 2 B. **(C)** Representative images of half spindles from spindle assembly reactions carried out in the presence of DMSO, 50 µM CK2i, 300 µM importazole or 50 µM CK2i and 300 µM importazole, as indicated. β-tubulin (magenta), DNA (cyan), TPX2 (green). **(D)** Representative images of half spindles from spindle assembly reactions carried out in the presence of DMSO and XB (control), 50 µM CK2i and XB (CK2i), 2.5 µM importin-β(71–876) and DMSO (Impβ[71–876]), or 50 µM CK2i and 2.5 µM importin-β(71–876) (CK2i + Impβ[71–876]), as indicated. β-tubulin (magenta), DNA (cyan), and TPX2 (green). **(E)** Violin plot of half spindle length of half spindles from experiment described in (C). $n \geq 324$ half spindles per condition (from three cytoplasmic extracts [$n \geq 105$ per extract for each condition]). **(F and G)** Violin plot of β-tubulin (F) or TPX2 (G) intensity at spindle poles of half spindles from experiment described in C. $n \geq 420$ half spindles per condition (from three cytoplasmic extracts [$n \geq 133$ per extract for each condition]). **(H)** Violin plot of half spindle length of half spindles from experiment described in D. $n \geq 313$ half spindles per condition (from three cytoplasmic extracts [$n \geq 104$ per extract for each condition]). **(I and J)** Violin plot of β-tubulin (I) or TPX2 (J) intensity at spindle poles of half spindles from experiment described in D. $n \geq 329$ half spindles per condition (from three cytoplasmic extracts [$n \geq 92$ per extract for each condition]). **(K)** Schematic illustrating how the Ran pathway of spindle assembly may be altered by the decrease in CK2 activity at fertilization. Microtubules (magenta), DNA (cyan), activated Ran pathway (orange), TPX2 and other Ran-regulated SAFs (green). Where the Ran pathway is highly active, SAFs are released from importins and drive localized microtubule nucleation and stabilization. In meiosis, Ran pathway activation is limited to a small region surrounding chromosomes. In mitosis, Ran pathway activation extends to a broader area, leading to increased localization of TPX2 and other Ran-regulated SAFs, including ELYS and augmin, at spindle poles, increasing spindle length and driving astral microtubule polymerization at spindle poles. Statistical significance was determined by two-tailed Mann–Whitney tests (**** = P < 0.00005). For violin plots, lines indicate the median and upper and lower quartiles.

gelatin-coated petri dish. Eggs were mixed with sperm for 3 min and then dechorionated by mixing with dechorionation solution (0.1 g/ml sodium thioglycolate, 0.01 g/ml protease [*Streptomyces griseus*] [Cat# PP8811; Sigma-Aldrich], and 0.06 M NaOH) and then washed three times with artificial seawater, and embryos maintained at 16°C.

Xenopus husbandry, gamete collection, and in vitro fertilization

Mature *X. laevis* were obtained from *Xenopus*1 or the National *Xenopus* Resource (Woods Hole) and maintained and used following standard protocols in the Animal Use Protocol approved by the UC Berkeley Animal Care and Use Committee. J-strain (backcrossed) *X. laevis* (National *Xenopus* Resource) were used to prepare samples for all proteomic and phosphoproteomic experiments. Testes were dissected from adult males and stored at 4°C in MR (100 mM NaCl, 1.8 mM KCl, 1 mM $MgCl_2$, 2 mM $CaCl_2$, and 5 mM HEPES [pH 7.6]) for <1 wk. Females were primed by injection with 100 U of pregnant mare serum gonadotropin (National Hormone and Peptide Program) at least 48 h before use and boosted by injection with 500 U of human chorionic gonadotropin 16 h before use. Females were gently squeezed to deposit eggs into petri dishes. 1/3 of a testis was homogenized using scissors and a plastic pestle in 1.1 ml ddH_2O in a 1.5-ml tube, then added to the petri dish of eggs and swirled to mix and incubated for 5–10 min. Dishes were flooded with 0.1X MMR (100 mM NaCl, 2 mM KCl, 1 mM $MgCl_2$, 2 mM $CaCl_2$, 5 mM HEPES [pH 7.6], and 0.1 mM EDTA) and incubated for 10 min. Jelly coats were removed by incubation in 2% cysteine solution (in ddH_2O-NaOH [pH 7.8]), then embryos were washed at least four times in 0.1X MMR and incubated at 23°C. *Xenopus* illustrations were obtained from Xenbase (https://www.xenbase.org, RRID:SCR_003280).

Xenopus egg and embryo extract preparation and spindle assembly reactions

X. laevis crude CSF egg extracts were prepared as described previously (Maresca and Heald, 2006). Briefly, eggs were packed using a clinical tabletop centrifuge and then crushed by centrifugation for 16 min at 10,200 rpm (max 17,048 rcf) (16°C) in an HB-6 rotor (Sorvall). Cytoplasm was removed and supplemented with 20 µg/ml cytochalasin B (Cyto B); 10 µg/ml leupeptin, pepstatin, and chymostatin; and 1X energy mix (3.75 mM creatine phosphate, 0.5 mM ATP, 0.05 mM EGTA, and 0.5 mM $MgCl_2$). Stage 8 embryo extracts were prepared as described previously (Wilbur and Heald, 2013). Briefly, embryos maintained for 5.5 h after fertilization at 23°C were washed extensively in CSF-XB (5 mM EGTA, 100 mM KCl, 2 mM $MgCl_2$, 0.1 mM $CaCl_2$, 50 mM sucrose, and 10 mM HEPES [pH 7.8]) supplemented with 20 µg/ml Cyto B and packed by centrifugation at 215 rcf for 1 min and then 860 rcf for 30 s in a microcentrifuge at 16°C and then crushed by centrifugation for 12 min at 10,200 rpm (max 17,048 rcf) (16°C) in an HB-6 rotor (Sorvall). Cytoplasm was removed and supplemented with 20 µg/ml Cyto B; 10 µg/ml leupeptin, pepstatin, and chymostatin; 1X energy mix; 0.2 mg/ml UbcH10 C114S; and 0.05 mg/ml cyclin B delta 90.

For spindle assembly reactions, purified *X. laevis* sperm nuclei were added to egg and embryo extracts at a concentration of 1,000 nuclei/µl. To visualize microtubules, extracts were supplemented with 0.3 µM rhodamine-labeled tubulin. Tubulin was prepared from porcine brains by two cycles of polymerization then labeled with rhodamine (Cat# 90005; Biotium) (Hyman et al., 1991). For sample preparation for proteomic and phosphoproteomic analysis, rhodamine-labeled tubulin was not added, but spindle assembly was monitored by microscopy in a parallel test reaction, using the same extract and conditions, labeled with rhodamine-tubulin.

Fixation, immunofluorescence, and imaging

C. robusta eggs and embryos were fixed overnight at 4°C in "von Dassow fixative" (100 mM HEPES [pH 7], 50 mM EGTA [pH 7], 10 mM $MgSO_4$, 500 mM dextrose, 2% formaldehyde, 0.2% glutaraldehyde, and 0.2% Triton X-100) (Crowder et al., 2015) in 5% BSA-coated tubes, washed three times in PBS, 0.1% Triton X-100 (PBT), once in PBS, and incubated in 0.1% $NaBH_4$ in PBS. For

immunofluorescence, *Ciona* samples were blocked (5% normal goat serum, 0.2% BSA in PBT) overnight at 4°C, incubated in primary antibody (1.25 µg/ml E7 anti–β-tubulin [Cat# E7; DSHB, RRID:AB_528499] in PBT + 0.2% BSA) for 72 h at RT, washed for 24 h in PBT + 0.2% BSA, incubated in secondary antibody (2 µg/ml goat anti-mouse Alexa Fluor 568 [Cat# A-11004; Molecular Probes, RRID:AB_2534072]) for 72 h at RT, washed for 24 h in PBT + 0.2% BSA, incubated in 1 µg/ml Hoechst 33342 (Cat# H3570; Thermo Fisher Scientific) in PBT + 0.2% BSA for 30 min at RT, washed three times in PBT, and then mounted in Vectashield (Vector Labs) between tape spacers on a glass slide. Samples were imaged using a Zeiss PlanApo 63x (NA 1.4) oil or Zeiss PlanApo 20x (NA 0.8) air objective at RT on a Zeiss LSM 800 confocal microscope (ZEN 2.3 software) with 488 and 568 laser lines. Egg and zygote cell diameter and spindle length (outer edge of aster to outer edge of aster) measurements were made using Imaris 9.5.1 (RRID:SCR_007370).

X. laevis eggs and embryos were fixed for 1–3 h at RT in MAD fixative (40% MeOH, 40% acetone, and 20% DMSO) and then stored at −20°C. Samples were gradually rehydrated into 0.5X SSC (75 mM NaCl and 15 mM sodium citrate, pH 7), then bleached under direct light in bleaching solution (2% H_2O_2 and 5% formamide in 0.5X SSC) for 2–3 h and washed twice in PBT. Samples were blocked in 10% normal goat serum + 5% DMSO in PBT overnight at 4°C, then incubated at 4°C for 24 h in primary antibodies (1.25 µg/ml E7 anti–β-tubulin [Cat# E7; DSHB, RRID:AB_528499] and 2 µg/ml ab1791 anti-H3 [Cat# ab1791; Abcam, RRID:AB_302613] in PBT + 10% normal goat serum), washed for 24 h in PBT, incubated for 24 h at 4°C in secondary antibodies (4 µg/ml goat anti-mouse Alexa Fluor 568 [Cat# A-11004; Molecular Probes, RRID:AB_2534072] and 4 µg/ml goat anti-rabbit Alexa Fluor 488 [Cat# A-11008; Thermo Fisher Scientific, RRID:AB_143165] in PBT), and then washed for 24 h in PBT. Samples were then gradually dehydrated into 100% MeOH, stored overnight at −20°C, then cleared by incubation in Murray's clear (two parts benzyl benzoate and one part benzyl alcohol), and then mounted on a glass coverslip. Samples were imaged using a Zeiss PlanApo 20x (NA 0.8) air objective on a Zeiss LSM 800 confocal microscope (ZEN 2.3 software) with 488 and 568 laser lines at RT. Egg and zygote cell diameter and spindle length measurements were made using Imaris 9.5.1. Cell diameter was measured across the widest part of cell. Spindle length was measured from outer edge of aster to outer edge of aster, or pole to pole for meiotic spindles with no asters present, along the long axis of the spindle.

Spindles and half spindles from *X. laevis* spindle assembly reactions were spun down onto coverslips and fixed as described previously (Hannak and Heald, 2006). Briefly, spindles or half spindles were fixed in spindle dilution buffer (30% glycerol, 1 X BRB80 [80 mM PIPES [pH 6.8], 1 mM $MgCl_2$, and 1 mM EGTA], 0.5% Triton X-100, and 3.7% formaldehyde) and then spun down onto glass coverslips through a cushion (40% glycerol and 1X BRB80) by centrifugation for 20 min at 5,500 rpm (max 5,838 rcf) (16°C) in an HS-4 rotor (Sorvall). Coverslips were postfixed for 5 min in cold 100% methanol and then washed in PBS NP40 (1X PBS and 0.1% NP40). For immunofluorescence, coverslips were blocked with PBS-BSA (1X PBS and 3% BSA) for 45 min at RT, incubated at 4°C overnight with primary antibody (1:4,000 rabbit–anti-TPX2 [Miller et al., 2019]) in PBS-BSA, washed with PBS-NP40, incubated for 1 h at RT with secondary antibody (4 µg/ml goat anti-rabbit Alexa Fluor 488 [Cat# A-11008; Thermo Fisher Scientific, RRID:AB_143165] in PBS-BSA), and then washed with PBS-NP40. To visualize DNA, coverslips were incubated for 1 min in 1 µg/ml Hoechst 33342 (Cat# H3570; Thermo Fisher Scientific) in PBS-NP40 and then washed with PBS-NP40. Coverslips were mounted in Vectashield (Vector Labs) on a glass slide and sealed with clear nail polish. Samples were imaged using an Olympus UPlan Fl 40X (NA 0.75) or Olympus UPlan Fl 20X (NA 0.5) air objective and Hamamatsu ORCA-ER camera or Hamamatsu ORCA-II camera on an Olympus BX51 widefield microscope (cellSens software) or a Zeiss Plan-Apochromat 40X (NA 0.95) air objective and Axiocam 712 camera on a Zeiss Axio Observer 7 widefield microscope (ZEN 3.6 software) (using Apotome 3 for representative images). Spindle and half spindle length measurements were made using Fiji (ImageJ) (RRID:SCR_003070). Spindle length was measured from outer edge of aster to outer edge of aster, or pole to pole for meiotic spindles with no asters present, along the long axis of the spindle. Half spindle length was measured as the distance from outer edge of the aster (or pole if no aster was present) to DNA. To quantify fluorescence intensity at spindle and half spindle poles, total fluorescence intensity in each channel was measured in a square (200 × 200 pixels) centered on each spindle pole, and total fluorescence intensity of a background square (200 × 200 pixels) was subtracted from it.

Drug treatments, protein additions, and immunodepletion

Ciona oocytes were bathed in artificial seawater containing the indicated concentration of silmitasertib (MedChem Express), importazole (Sigma-Aldrich), palmostatin (Millipore-Sigma), monastrol (Abcam), BI2536 (Selleck Chemicals), okadaic acid (Cayman Chemical Company), ZM447439 (Selleck Chemicals), or tozasertib (MedChem Express). For drug treatments of extracts, drug stocks were diluted 1:5 in XB (1 mM $MgCl_2$, 0.1 mM $CaCl_2$, 100 mM KCl, 50 mM sucrose, and 10 mM HEPES [pH 7.7]) and added at the beginning of the spindle assembly reaction. 4,5,6,7-tetrabromobenzotriazole was purchased from Selleck Chemicals. For protein addition to extracts, proteins were in XB, and an equal volume of XB was added to the control reaction.

Immunodepletion of CK2 from *X. laevis* egg extracts was carried out as described previously (Hannak and Heald, 2006). Briefly, 50 µl Protein A Dynabeads (Thermo Fisher Scientific) were co-conjugated to 20 µg anti-CK2α antibody (Cat# sc-373894; Santa Cruz Biotechnology, RRID:AB_10947405) and 10 µg anti-CK2β antibody (Cat# sc-12739; Santa Cruz Biotechnology, RRID:AB_626792) or 30 µg mouse IgG isotype control (Cat# 10400C; Thermo Fisher Scientific, RRID:AB_2532980). 75 µl of extract was incubated with 25 µl of beads for 45 min on ice with intermittent agitation twice before spindle assembly reactions. Protein concentration of CK2α following immunodepletion was assessed by western blot. Total protein concentration of the extract samples was determined by Pierce BCA assay (Thermo Fisher Scientific), and then 10 µg protein in Laemmli sample buffer was run on 4–20% Mini-PROTEAN polyacrylamide

gels (Bio-Rad). Proteins were transferred onto nitrocellulose membranes at 60 V at 4°C, blocked at RT with 4% milk in PBS, 0.1% Tween 20 (PBST), and incubated overnight at 4°C with primary antibodies (1:200 anti-CK2α antibody [Cat# sc-373894; Santa Cruz Biotechnology, RRID:AB_10947405] or 1:500 anti-Vinculin antibody Cat# MA1–90508; Thermo Fisher Scientific, RRID:AB_2214494). Following washes in PBST, blots were incubated with secondary antibody (1:10,000 IRDye 680RD goat anti-mouse IgG [Cat# 926–68180; LI-COR Biosciences, RRID: AB_281492]) for 1.5 h at RT, washed again with PBST, and then imaged on an Odyssey CLx imager (LI-COR) (700 channel). Band intensities were measured using Fiji (ImageJ).

CK2 activity assay

For *X. laevis* lysates, 10 dejellied eggs or zygotes of the appropriate stage (confirmed by immunofluorescence of parallel samples taken at the same time point after fertilization) were snap frozen. Samples were resuspended in 50 µl of *Xenopus* lysis buffer (25 mM HEPES [pH 7.2], 10 mM EDTA, 250 mM sucrose, 1% NP40, 1 tablet/10 ml PhosSTOP [EDTA-free] [Roche], 1 tablet/10 ml cOmplete mini protease inhibitor [EDTA-free] [Roche], 0.2 mM PMSF, and 10 µM Cyto B) on ice and lysed by pipetting and then thorough vortexing. Yolk removal was carried out as previously described (Van Itallie et al., 2021, *Preprint*); samples were centrifuged at 4,000 *g* for 4 min (4°C) in a microcentrifuge, then lipids were resuspended by gentle flicking, and the supernatant was retained. Total protein concentration of samples was determined by Bradford assay (Bio-Rad), and samples were diluted to a concentration of 500 µg/ml. To determine CK2 activity, a CycLex CK2 Kinase Assay Kit (MBL Life Science) was used according to the manufacturer's recommended protocol.

For *C. robusta* lysates, dechorionated eggs or zygotes of the appropriate stage and from a fertilization with a fertilization efficiency of >79% (confirmed by immunofluorescence of parallel samples taken at the same time point after fertilization) were washed in PBS, pelleted by centrifugation at 845 rcf for 1 min (16°C) in a microcentrifuge, and snap frozen. Pellets were resuspended in 100 µl *Ciona* lysis buffer (20 mM Tris-HCl [pH 7.4], 1 mM EDTA [pH 8.0], 150 mM NaCl, 0.5% NP40, 1 tablet/10 ml PhosSTOP [EDTA-free] [Roche], 1 tablet/10 ml cOmplete mini protease inhibitor [EDTA-free] [Roche], and 0.2 mM PMSF) on ice, incubated for 5 min on ice, and then lysed with a plastic pestle for 1 min. Following centrifugation at 15,871 rcf for 5 min (4°C), the supernatant was retained. Total protein concentration of samples was determined by Bradford assay (Bio-Rad), and samples were diluted to a concentration of 500 µg/ml. To determine CK2 activity, a CycLex CK2 Kinase Assay Kit (MBL Life Science) was used according to the manufacturer's recommended protocol.

To assess CK2 activity following drug treatment of *X. laevis* extracts, the total protein concentration of the extract samples was determined by Pierce BCA assay (Thermo Fisher Scientific), and then samples were diluted to a concentration of 500 µg/ml before a CycLex CK2 Kinase Assay Kit (MBL Life Science) was used according to the manufacturer's recommended protocol. CK2 (alpha/beta)-positive control (MBL) was used for control assays.

Sample preparation for proteomics

For each of two experimental repeats, spindle assembly reactions were carried out in three independent meiotic egg extracts and three independent mitotic embryo extracts in the presence of 25 µM silmitasertib or DMSO (meiotic) or 10 µM silmitasertib or DMSO (mitotic). After 1-h incubation at 18°C, once spindles had formed, samples were snap frozen in liquid nitrogen and stored at −80°C. Total protein concentration of the sample was determined by Bradford assay (Bio-Rad). Reduction in kinase activity upon drug treatment of each sample was confirmed by a CK2 activity assay (CycLex CK2 Kinase Assay Kit [MBL Life Science]) on samples diluted 1:10 in XB. Metaphase arrest of each extract sample after 1-h spindle assembly reaction was confirmed by spindle spin down, fixation, and imaging as described above.

Proteins from egg and embryo extracts were precipitated with ice-cold acetone and resuspended in ice-cold lysis buffer (8 M urea, 25 mM Tris-HCl [pH 8.5], 150 mM NaCl, phosphatase inhibitors [2.5 mM β-glycerophosphate, 1 mM sodium fluoride, 1 mM sodium orthovanadate, and 1 mM sodium molybdate], and protease inhibitors 1 tablet/10 ml cOmplete mini protease inhibitor [EDTA-free] [Roche]) and sonicated three times for 15 s each with intermittent cooling on ice. Lysates were centrifuged at 15,000 rcf for 30 min at 4°C. A portion was removed to determine protein concentration by BCA assay (Pierce/Thermo Fisher Scientific). The remaining supernatants were reduced with 5 mM DTT at 55°C for 30 min, cooled to RT, and alkylated with 15 mM iodoacetamide at RT, in the dark, for 45 min. Alkylation reactions were quenched with an additional 5 mM of DTT for 10 min at RT and then diluted sixfold with 25 mM Tris (pH 8.1) before digestion with trypsin at a concentration of 1:100 (wt/wt) (Sigma-Aldrich) overnight at 37°C. The next day, digests were quenched by acidification with 0.25% TFA (vol/vol), centrifuged to remove precipitation, and desalted with an Oasis HLB 60 mg plate (Waters). For proteomics analysis, 40 µg of peptide digests from each sample were removed. The remaining peptides were lyophilized and stored at −80°C before further analysis.

Proteomics, phosphoproteomics, and data normalization

For proteomics analysis, peptides were labeled with TMTpro reagents (Thermo Fisher Scientific) in 100 mM EPPS (pH 8.5)/20% ACN at RT for 1 h before a small portion was removed from each sample to determine labeling efficiency. Labeling was confirmed to be at least 95% efficient before quenching with the addition of hydroxylamine to a final concentration of 0.25% for 10 min, mixed, acidified with TFA to a pH of about 2, and desalted over an Oasis HLB 10 mg plate (Waters). The desalted multiplex was dried by vacuum centrifugation and separated by offline pentafluorophenyl-based reversed-phase HPLC fractionation as previously described (Grassetti et al., 2017).

For phosphoproteomics analysis, lyophilized digested peptides were subjected to phosphopeptide enrichment with the High Select Fe-NTA Phosphopeptide Enrichment Kit (Thermo Fisher Scientific) following the manufacturer's instructions and desalted over an Oasis HLB 10 mg plate (Waters). Phosphopeptides were then labeled with TMTpro reagents and offline separated as described above.

TMT-labeled peptides were analyzed on an Orbitrap Lumos mass spectrometer (Thermo Fisher Scientific) equipped with an Easy-nLC 1,200 (Thermo Fisher Scientific). The raw data files were searched using COMET (Eng et al., 2013) with a static mass of 304.2071 Da on peptide N-termini and lysines, 57.02146 Da on cysteines, and a variable mass of 15.99491 Da on methionines and for phosphorylation 79.96633 Da on serines, threonines, and tyrosines against the target-decoy version (Elias and Gygi, 2007) of the annotated *X. laevis* proteome database (Xenbase, v9.2) (Fisher et al., 2023) and filtered to a <1% FDR at the peptide level. Quantification of LC-MS/MS spectra was performed using in-house developed software. The probability of phosphorylation site localization was determined by PhosphoRS (Taus et al., 2011). For proteomics analysis, peptide intensities were adjusted based on total TMT reporter ion intensity in each channel across all samples and $\log_2$ transformed. For phosphoproteomics analysis, peptide intensities were adjusted based on total TMT reporter ion intensity in each channel across all samples (or for phase-normalized data across meiotic samples or mitotic samples, respectively) and $\log_2$ transformed. P values were calculated using a two-tailed Student's *t* test in Perseus (Tyanova et al., 2016).

GO enrichment and network analysis

For analysis, proteomic and phosphoproteomic data from the two experimental repeats (total peptide count >1 filtered) were pooled. Data were annotated with human orthologs using the mapping to the *X. laevis* v9.2 genome in the files available at https://wuehr.scholar.princeton.edu/protein-concentrations-xenopus-egg (Wühr et al., 2014). GO enrichment analysis was carried out on human orthologs using PANTHER version 19.0 (Thomas et al., 2022) with default parameters. Network analysis was carried out on human orthologs using STRING version 12.0 (Szklarczyk et al., 2019) (RRID:SCR_005223) using full STRING network annotations with high confidence (interaction score ≥0.7). Edge color indicates data source, with known interactions shown in cyan (from curated databases) and magenta (experimentally determined), predicted interactions shown in emerald green (gene neighborhood), red (gene fusions), royal blue (gene co-occurrence), lime green (text mining), black (co-expression), and lilac (protein homology). K-means clustering with default parameters was used to define functional clusters.

Statistical tests

Mann–Whitney and *t* tests (as indicated in figure legends) were carried out using Prism 9.0 (RRID:SCR_002798). Linear regression analysis was carried out using Prism 10.0.

Online supplemental material

Fig. S1 shows that spindle length changes dramatically at the meiosis-to-mitosis transition in *Ciona* and *Xenopus*, though cell size does not. Fig. S2 shows the effects of small molecules on meiotic spindle morphology in *Ciona* oocytes and effects of CK2 inhibition on meiotic and mitotic X. *laevis* extracts. Fig. S3 shows that CK2 activity is reduced by CK2 inhibition in *X. laevis* extract. Fig. S4 shows the proteomic changes between meiosis and mitosis and upon CK2 inhibition. Fig. S5 shows the phosphoproteomic changes between meiosis and mitosis and upon CK2 inhibition. Fig. S6 shows that inhibition of the RanGTP-mediated spindle assembly pathway reduces TPX2 and tubulin intensity at spindle poles in *X. laevis* egg extracts. Table S1 shows the summary of the proteomic data. Table S2 shows the summary of the phosphoproteomic data. Table S3 shows the GO enrichment analysis results—proteins enriched in meiosis relative to mitosis. Table S4 shows the microtubule-binding proteins enriched in meiosis relative to mitosis. Table S5 shows the GO enrichment analysis results—proteins enriched in mitosis relative to meiosis. Table S6 shows the GO enrichment analysis results—proteins with phosphosites enriched in mitosis. Table S7 shows the proteins in spindle GO category (GO:0005819) with phosphosites enriched in mitosis relative to meiosis. Table S8 shows the candidate proteins annotated with localization data.

Data availability

Mass spectrometry data are available at ProteomeXchange: PXD053646 and MassIVE: MSV000095250. All other data are available from the corresponding authors upon request.

Acknowledgments

We thank Matthew Swaffer, Coral Zhou, Xiao Liu, Gabriel Cavin-Meza, Cordell Clark and Alex Lessenger for feedback on the manuscript; Yasaswini Sampathkumar for importin-β(71–876) protein; Michael Levine and Laurence Lemaire for training and advice on *Ciona* experiments; and Marina Crowder for advice.

This work was supported by the National Institutes of Health MIRA grant R35GM118183 and the Flora Lamson Hewlett Chair in Biochemistry to R. Heald, an EMBO long-term postdoctoral fellowship to H. Cantwell, and National Institute of General Medical Sciences grant R35GM119455 to A.N. Kettenbach.

Author contributions: H. Cantwell: conceptualization, formal analysis, funding acquisition, investigation, methodology, visualization, and writing—original draft, review, and editing. H. Nguyen: formal analysis and investigation. A.N. Kettenbach: data curation, formal analysis, funding acquisition, investigation, project administration, resources, software, supervision, and writing—review and editing. R. Heald: conceptualization, funding acquisition, project administration, resources, supervision, validation, and writing—review and editing.

Disclosures: The authors declare no competing interests exist.

Submitted: 25 July 2024
Revised: 30 April 2025
Accepted: 27 May 2025

References

Askjaer, P., A. Bachi, M. Wilm, F.R. Bischoff, D.L. Weeks, V. Ogniewski, M. Ohno, C. Niehrs, J. Kjems, I.W. Mattaj, et al. 1999. RanGTP-Regulated interactions of CRM1 with nucleoporins and a shuttling DEAD-Box helicase. *Mol. Cell. Biol.* 19:6276–6285. https://doi.org/10.1128/MCB.19.9.6276

Avilov, I., Y. Horokhovskyi, M. Cai, A. Orzechowski, L. Welp, H. Urlaub, J. Liepe, and P. Lenart. 2023. Phosphoproteomics identifies targets of

Mos-MAPK regulating translation and spindle organization in oocyte meiosis. *bioRxiv*. https://doi.org/10.1101/2023.11.27.568807 (Preprint posted November 27, 2023).
Bennabi, I., I. Quéguiner, A. Kolano, T. Boudier, P. Mailly, M.-H. Verlhac, and M.-E. Terret. 2018. Shifting meiotic to mitotic spindle assembly in oocytes disrupts chromosome alignment. *EMBO Rep.* 19:368–381. https://doi.org/10.15252/embr.201745225
Blow, J.J. 2003. A new role for ran in ensuring precise duplication of chromosomal DNA. *Cell*. 113:2–4. https://doi.org/10.1016/S0092-8674(03)00236-8
Bomar, J., P. Moreira, J.J. Balise, and P. Collas. 2002. Differential regulation of maternal and paternal chromosome condensation in mitotic zygotes. *J. Cell Sci.* 115:2931–2940. https://doi.org/10.1242/jcs.115.14.2931
Borgo, C., C. D'Amore, S. Sarno, M. Salvi, and M. Ruzzene. 2021. Protein kinase CK2: A potential therapeutic target for diverse human diseases. *Signal Transduct. Target. Ther.* 6:183. https://doi.org/10.1038/s41392-021-00567-7
Brownlee, C., and R. Heald. 2019. Importin α partitioning to the plasma membrane regulates intracellular scaling. *Cell*. 176:805–815.e8. https://doi.org/10.1016/j.cell.2018.12.001
Carazo-Salas, R.E., G. Guarguaglini, O.J. Gruss, A. Segref, E. Karsenti, and I.W. Mattaj. 1999. Generation of GTP-bound Ran by RCC1 is required for chromatin-induced mitotic spindle formation. *Nature*. 400:178–181. https://doi.org/10.1038/22133
Caudron, M., G. Bunt, P. Bastiaens, and E. Karsenti. 2005. Spatial coordination of spindle assembly by chromosome-mediated signaling gradients. *Science*. 309:1373–1376. https://doi.org/10.1126/science.1115964
Cavazza, T., I. Peset, and I. Vernos. 2016. From meiosis to mitosis – The sperm centrosome defines the kinetics of spindle assembly after fertilization in *Xenopus*. *Development*. 143:e1.1. https://doi.org/10.1242/dev.141796
Cavazza, T., Y. Takeda, A.Z. Politi, M. Aushev, P. Aldag, C. Baker, M. Choudhary, J. Bucevičius, G. Lukinavičius, K. Elder, et al. 2021. Parental genome unification is highly error-prone in mammalian embryos. *Cell*. 184:2860–2877.e22. https://doi.org/10.1016/j.cell.2021.04.013
Cavazza, T., and I. Vernos. 2016. The RanGTP pathway: From nucleo-cytoplasmic transport to spindle assembly and beyond. *Front. Cell Dev. Biol.* 3:82. https://doi.org/10.3389/fcell.2015.00082
Cesario, J., and K.S. McKim. 2011. RanGTP is required for meiotic spindle organization and the initiation of embryonic development in *Drosophila*. *J. Cell Sci.* 124:3797–3810. https://doi.org/10.1242/jcs.084855
Christiaen, L., E. Wagner, W. Shi, and M. Levine. 2009a. The sea squirt *Ciona intestinalis*. *Cold Spring Harb. Protoc.* 2009:pdb.emo138. https://doi.org/10.1101/pdb.emo138
Christiaen, L., E. Wagner, W. Shi, and M. Levine. 2009b. Isolation of sea squirt (*Ciona*) gametes, fertilization, dechorionation, and development. *Cold Spring Harb. Protoc.* 2009:pdb.prot5344. https://doi.org/10.1101/pdb.prot5344
Colombié, N., C.F. Cullen, A.L. Brittle, J.K. Jang, W.C. Earnshaw, M. Carmena, K. McKim, and H. Ohkura. 2008. Dual roles of incenp crucial to the assembly of the acentrosomal metaphase spindle in female meiosis. *Development*. 135:3239–3246. https://doi.org/10.1242/dev.022624
Coticchio, G., D. Cimadomo, G.C. Cermisoni, L. Rienzi, E. Papaleo, F.M. Ubaldi, A. Borini, and L. De Santis. 2023. The first mitotic division: A perilous bridge connecting the zygote and the early embryo. *Hum. Reprod.* 38:1019–1027. https://doi.org/10.1093/humrep/dead067
Courtois, A., M. Schuh, J. Ellenberg, and T. Hiiragi. 2012. The transition from meiotic to mitotic spindle assembly is gradual during early mammalian development. *J. Cell Biol.* 198:357–370. https://doi.org/10.1083/jcb.201202135
Crowder, M.E., M. Strzelecka, J.D. Wilbur, M.C. Good, G. von Dassow, and R. Heald. 2015. A comparative analysis of spindle morphometrics across metazoans. *Curr. Biol.* 25:1542–1550. https://doi.org/10.1016/j.cub.2015.04.036
Currie, C.E., E. Ford, L. Benham Whyte, D.M. Taylor, B.P. Mihalas, M. Erent, A.L. Marston, G.M. Hartshorne, and A.D. McAinsh. 2022. The first mitotic division of human embryos is highly error prone. *Nat. Commun.* 13:6755. https://doi.org/10.1038/s41467-022-34294-6
De Almeida, M., M. Hinterndorfer, H. Brunner, I. Grishkovskaya, K. Singh, A. Schleiffer, J. Jude, S. Deswal, R. Kalis, M. Vunjak, et al. 2021. AKIRIN2 controls the nuclear import of proteasomes in vertebrates. *Nature*. 599:491–496. https://doi.org/10.1038/s41586-021-04035-8
Drutovic, D., X. Duan, R. Li, P. Kalab, and P. Solc. 2020. RanGTP and importin β regulate meiosis I spindle assembly and function in mouse oocytes. *EMBO J.* 39:e101689. https://doi.org/10.15252/embj.2019101689
Dumont, J., S. Petri, F. Pellegrin, M.-E. Terret, M.T. Bohnsack, P. Rassinier, V. Georget, P. Kalab, O.J. Gruss, and M.-H. Verlhac. 2007. A centriole- and RanGTP-independent spindle assembly pathway in meiosis I of vertebrate oocytes. *J. Cell Biol.* 176:295–305. https://doi.org/10.1083/jcb.200605199
Dupré, A., O. Haccard, and C. Jessus. 2011. Mos in the oocyte: How to use MAPK independently of growth factors and transcription to control meiotic divisions. *J. Signal Transduct.* 2011:350412. https://doi.org/10.1155/2011/350412
Elias, J.E., and S.P. Gygi. 2007. Target-decoy search strategy for increased confidence in large-scale protein identifications by mass spectrometry. *Nat. Methods*. 4:207–214. https://doi.org/10.1038/nmeth1019
Ems-McClung, S.C., M. Emch, S. Zhang, S. Mahnoor, L.N. Weaver, and C.E. Walczak. 2020. RanGTP induces an effector gradient of XCTK2 and importin α/β for spindle microtubule cross-linking. *J. Cell Biol.* 219:e201906045. https://doi.org/10.1083/jcb.201906045
Ems-McClung, S.C., Y. Zheng, and C.E. Walczak. 2004. Importin α/β and RanGTP regulate XCTK2 microtubule binding through a bipartite nuclear localization signal. *Mol. Biol. Cell*. 15:46–57. https://doi.org/10.1091/mbc.e03-07-0454
Eng, J.K., T.A. Jahan, and M.R. Hoopmann. 2013. Comet: An open-source MS/MS sequence database search tool. *Proteomics*. 13:22–24. https://doi.org/10.1002/pmic.201200439
Fisher, M., C. James-Zorn, V. Ponferrada, A.J. Bell, N. Sundararaj, E. Segerdell, P. Chaturvedi, N. Bayyari, S. Chu, T. Pells, et al. 2023. Xenbase: Key features and resources of the *Xenopus* model organism knowledgebase. *Genetics*. 224:iyad018. https://doi.org/10.1093/genetics/iyad018
Gadea, B.B., and J.V. Ruderman. 2006. Aurora B is required for mitotic chromatin-induced phosphorylation of Op18/Stathmin. *Proc. Natl. Acad. Sci. USA*. 103:4493–4498. https://doi.org/10.1073/pnas.0600702103
Grassetti, A.V., R. Hards, and S.A. Gerber. 2017. Offline pentafluorophenyl (PFP)-RP prefractionation as an alternative to high-pH RP for comprehensive LC-MS/MS proteomics and phosphoproteomics. *Anal. Bioanal. Chem.* 409:4615–4625. https://doi.org/10.1007/s00216-017-0407-6
Gruss, O.J., R.E. Carazo-Salas, C.A. Schatz, G. Guarguaglini, J. Kast, M. Wilm, N. Le Bot, I. Vernos, E. Karsenti, and I.W. Mattaj. 2001. Ran induces spindle assembly by reversing the inhibitory effect of importin α on TPX2 activity. *Cell*. 104:83–93. https://doi.org/10.1016/s0092-8674(01)00193-3
Gruss, O.J., and I. Vernos. 2004. The mechanism of spindle assembly: Functions of Ran and its target TPX2. *J. Cell Biol.* 166:949–955. https://doi.org/10.1083/jcb.200312112
Hachet, V., T. Köcher, M. Wilm, and I.W. Mattaj. 2004. Importin α associates with membranes and participates in nuclear envelope assembly in vitro. *EMBO J.* 23:1526–1535. https://doi.org/10.1038/sj.emboj.7600154
Hannak, E., and R. Heald. 2006. Investigating mitotic spindle assembly and function in vitro using *Xenopus laevis* egg extracts. *Nat. Protoc.* 1:2305–2314. https://doi.org/10.1038/nprot.2006.396
Heald, R., R. Tournebize, T. Blank, R. Sandaltzopoulos, P. Becker, A. Hyman, and E. Karsenti. 1996. Self-organization of microtubules into bipolar spindles around artificial chromosomes in *Xenopus* egg extracts. *Nature*. 382:420–425. https://doi.org/10.1038/382420a0
Helmke, K.J., R. Heald, and J.D. Wilbur. 2013. Interplay between Spindle Architecture and Function. *In International Review of Cell and Molecular Biology*. Vol. 306. K.W. Jeon, editor. Elsevier, Amsterdam. 83–125.
Hodgson, B., A. Li, S. Tada, and J.J. Blow. 2002. Geminin becomes activated as an inhibitor of Cdt1/RLF-B following nuclear import. *Curr. Biol.* 12:678–683. https://doi.org/10.1016/S0960-9822(02)00778-9
Huang, Z., L. Ma, Y. Wang, Z. Pan, J. Ren, Z. Liu, and Y. Xue. 2015. MiCroKiTS 4.0: A database of midbody, centrosome, kinetochore, telomere and spindle. *Nucleic Acids Res.* 43:D328–D334. https://doi.org/10.1093/nar/gku1125
Hutten, S., and R.H. Kehlenbach. 2006. Nup214 is required for CRM1-Dependent nuclear protein export in vivo. *Mol. Cell. Biol.* 26:6772–6785. https://doi.org/10.1128/MCB.00342-06
Hyman, A., D. Drechsel, D. Kellogg, S. Salser, K. Sawin, P. Steffen, L. Wordeman, and T. Mitchison. 1991. Preparation of modified tubulins. *Methods Enzymol.* 196:478–485. https://doi.org/10.1016/0076-6879(91)96041-o
Kalab, P., and R. Heald. 2008. The RanGTP gradient – A GPS for the mitotic spindle. *J. Cell Sci.* 121:1577–1586. https://doi.org/10.1242/jcs.005959
Kalab, P., R.T. Pu, and M. Dasso. 1999. The Ran GTPase regulates mitotic spindle assembly. *Curr. Biol.* 9:481–484. https://doi.org/10.1016/S0960-9822(99)80213-9

Kalab, P., K. Weis, and R. Heald. 2002. Visualization of a Ran-GTP gradient in interphase and mitotic *Xenopus* egg extracts. *Science*. 295:2452–2456. https://doi.org/10.1126/science.1068798

Kelly, A.E., S.C. Sampath, T.A. Maniar, E.M. Woo, B.T. Chait, and H. Funabiki. 2007. Chromosomal enrichment and activation of the Aurora B pathway are coupled to spatially regulate spindle assembly. *Dev. Cell*. 12: 31–43. https://doi.org/10.1016/j.devcel.2006.11.001

Kimura, M., Y. Morinaka, K. Imai, S. Kose, P. Horton, and N. Imamoto. 2017. Extensive cargo identification reveals distinct biological roles of the 12 importin pathways. *Elife*. 6:e21184. https://doi.org/10.7554/eLife.21184

Kiyomitsu, A., T. Nishimura, S.J. Hwang, S. Ansai, M.T. Kanemaki, M. Tanaka, and T. Kiyomitsu. 2024. Ran-GTP assembles a specialized spindle structure for accurate chromosome segregation in medaka early embryos. *Nat. Commun.* 15:981. https://doi.org/10.1038/s41467-024-45251-w

Kraus, J., R. Alfaro-Aco, B. Gouveia, and S. Petry. 2023. Microtubule nucleation for spindle assembly: One molecule at a time. *Trends Biochem. Sci.* 48:761–775. https://doi.org/10.1016/j.tibs.2023.06.004

Kubiak, J.Z., M.A. Ciemerych, A. Hupalowska, M. Sikora-Polaczek, and Z. Polanski. 2008. On the transition from the meiotic to mitotic cell cycle during early mouse development. *Int. J. Dev. Biol.* 52:201–217. https://doi.org/10.1387/ijdb.072337jk

Lee, A., and A.A. Kiessling. 2017. Early human embryos are naturally aneuploid—can that be corrected? *J. Assist. Reprod. Genet.* 34:15–21. https://doi.org/10.1007/s10815-016-0845-7

Lindsay, L.L., J.C. Yang, and J.L. Hedrick. 1999. Ovochymase, a *Xenopus laevis* egg extracellular protease, is translated as part of an unusual polyprotease. *Proc. Natl. Acad. Sci. USA*. 96:11253–11258. https://doi.org/10.1073/pnas.96.20.11253

Manandhar, G., H. Schatten, and P. Sutovsky. 2005. Centrosome reduction during gametogenesis and its significance. *Biol. Reprod.* 72:2–13. https://doi.org/10.1095/biolreprod.104.031245

Maresca, T.J., A.C. Groen, J.C. Gatlin, R. Ohi, T.J. Mitchison, and E.D. Salmon. 2009. Spindle assembly in the absence of a RanGTP gradient requires localized CPC activity. *Curr. Biol.* 19:1210–1215. https://doi.org/10.1016/j.cub.2009.05.061

Maresca, T.J., and R. Heald. 2006. Methods for studying spindle assembly and chromosome condensation in *Xenopus* egg extracts. *In Xenopus Protocols*. X.J. Liu, editor. Humana Press, Totowa. 459–474.

Meggio, F., and L.A. Pinna. 2003. One-thousand-and-one substrates of protein kinase CK2? *FASEB J.* 17:349–368. https://doi.org/10.1096/fj.02-0473rev

Miesch, J., R.T. Wimbish, M.-C. Velluz, and C. Aumeier. 2023. Phase separation of +TIP networks regulates microtubule dynamics. *Proc. Natl. Acad. Sci. USA*. 120:e2301457120. https://doi.org/10.1073/pnas.2301457120

Miller, K.E., A.M. Session, and R. Heald. 2019. Kif2a scales meiotic spindle size in Hymenochirus boettgeri. *Curr. Biol.* 29:3720–3727.e5. https://doi.org/10.1016/j.cub.2019.08.073

Nachury, M.V., T.J. Maresca, W.C. Salmon, C.M. Waterman-Storer, R. Heald, and K. Weis. 2001. Importin β is a mitotic target of the small GTPase ran in spindle assembly. *Cell*. 104:95–106. https://doi.org/10.1016/s0092-8674(01)00194-5

Nishizawa, M., N. Furuno, K. Okazaki, H. Tanaka, Y. Ogawa, and N. Sagata. 1993. Degradation of Mos by the N-terminal proline (Pro2)-dependent ubiquitin pathway on fertilization of *Xenopus* eggs: Possible significance of natural selection for Pro2 in Mos. *EMBO J.* 12:4021–4027. https://doi.org/10.1002/j.1460-2075.1993.tb06080.x

Oakley, B.R., V. Paolillo, and Y. Zheng. 2015. γ-Tubulin complexes in microtubule nucleation and beyond. *Mol. Biol. Cell*. 26:2957–2962. https://doi.org/10.1091/mbc.E14-11-1514

Oh, D., C.-H. Yu, and D.J. Needleman. 2016. Spatial organization of the Ran pathway by microtubules in mitosis. *Proc. Natl. Acad. Sci. USA*. 113: 8729–8734. https://doi.org/10.1073/pnas.1607498113

Ohba, T., M. Nakamura, H. Nishitani, and T. Nishimoto. 1999. Self-organization of microtubule asters induced in *Xenopus* egg extracts by GTP-bound ran. *Science*. 284:1356–1358. https://doi.org/10.1126/science.284.5418.1356

Peshkin, L., A. Lukyanov, M. Kalocsay, R.M. Gage, D. Wang, T.J. Pells, K. Karimi, P.D. Vize, M. Wühr, and M.W. Kirschner. 2019. The protein repertoire in early vertebrate embryogenesis. *bioRxiv*. https://doi.org/10.1101/571174. (Preprint posted March 11, 2019).

Petry, S., A.C. Groen, K. Ishihara, T.J. Mitchison, and R.D. Vale. 2013. Branching microtubule nucleation in *Xenopus* egg extracts mediated by Augmin and TPX2. *Cell*. 152:768–777. https://doi.org/10.1016/j.cell.2012.12.044

Peuchen, E.H., O.F. Cox, L. Sun, A.S. Hebert, J.J. Coon, M.M. Champion, N.J. Dovichi, and P.W. Huber. 2017. Phosphorylation dynamics dominate the regulated proteome during early *Xenopus* development. *Sci. Rep.* 7:15647. https://doi.org/10.1038/s41598-017-15936-y

Rao, S.R., N. Flores-Rodriguez, S.L. Page, C. Wong, P.J. Robinson, and M. Chircop. 2016. The clathrin-dependent spindle proteome. *Mol. Cell. Proteomics* 15:2537–2553. https://doi.org/10.1074/mcp.M115.054809

Rieckhoff, E.M., F. Berndt, M. Elsner, S. Golfier, F. Decker, K. Ishihara, and J. Brugués. 2020. Spindle scaling is governed by cell boundary regulation of microtubule nucleation. *Curr. Biol.* 30:4973–4983.e10. https://doi.org/10.1016/j.cub.2020.10.093

Rosas-Salvans, M., T. Cavazza, G. Espadas, E. Sabido, and I. Vernos. 2018. Proteomic profiling of microtubule self-organization in M-phase. *Mol. Cell. Proteomics* 17:1991–2004. https://doi.org/10.1074/mcp.RA118.000745

Ruchaud, S., M. Carmena, and W.C. Earnshaw. 2007. Chromosomal passengers: Conducting cell division. *Nat. Rev. Mol. Cell Biol.* 8:798–812. https://doi.org/10.1038/nrm2257

Russo, G.L., M. Tosto, A. Mupo, I. Castellano, A. Cuomo, and E. Tosti. 2004. Biochemical and functional characterization of protein kinase CK2 in ascidian Ciona intestinalis oocytes at fertilization. Cloning and sequence analysis of cDNA for alpha and beta subunits. *J. Biol. Chem.* 279: 33012–33023. https://doi.org/10.1074/jbc.M401085200

Sampath, S.C., R. Ohi, O. Leismann, A. Salic, A. Pozniakovski, and H. Funabiki. 2004. The chromosomal passenger complex is required for chromatin-induced microtubule stabilization and spindle assembly. *Cell*. 118:187–202. https://doi.org/10.1016/j.cell.2004.06.026

Schneider, I., M. de Ruijter-Villani, M.J. Hossain, T.A.E. Stout, and J. Ellenberg. 2021. Dual spindles assemble in bovine zygotes despite the presence of paternal centrosomes. *J. Cell Biol.* 220:e202010106. https://doi.org/10.1083/jcb.202010106

Scrofani, J., T. Sardon, S. Meunier, and I. Vernos. 2015. Microtubule nucleation in mitosis by a RanGTP-Dependent protein complex. *Curr. Biol.* 25: 131–140. https://doi.org/10.1016/j.cub.2014.11.025

So, C., K.B. Seres, A.M. Steyer, E. Mönnich, D. Clift, A. Pejkovska, W. Möbius, and M. Schuh. 2019. A liquid-like spindle domain promotes acentrosomal spindle assembly in mammalian oocytes. *Science*. 364: eaat9557. https://doi.org/10.1126/science.aat9557

Soderholm, J.F., S.L. Bird, P. Kalab, Y. Sampathkumar, K. Hasegawa, M. Uehara-Bingen, K. Weis, and R. Heald. 2011. Importazole, a small molecule inhibitor of the transport receptor Importin-β. *ACS Chem. Biol.* 6: 700–708. https://doi.org/10.1021/cb2000296

Sukackaite, R., D. Cornacchia, M.R. Jensen, P.J. Mas, M. Blackledge, E. Enervald, G. Duan, T. Auchynnikava, M. Köhn, D.J. Hart, et al. 2017. Mouse Rif1 is a regulatory subunit of protein phosphatase 1 (PP1). *Sci. Rep.* 7: 2119. https://doi.org/10.1038/s41598-017-01910-1

Szklarczyk, D., A.L. Gable, D. Lyon, A. Junge, S. Wyder, J. Huerta-Cepas, M. Simonovic, N.T. Doncheva, J.H. Morris, P. Bork, et al. 2019. STRING v11: Protein–protein association networks with increased coverage, supporting functional discovery in genome-wide experimental datasets. *Nucleic Acids Res.* 47:D607–D613. https://doi.org/10.1093/nar/gky1131

Tachibana-Konwalski, K., J. Godwin, L. van der Weyden, L. Champion, N.R. Kudo, D.J. Adams, and K. Nasmyth. 2010. Rec8-containing cohesin maintains bivalents without turnover during the growing phase of mouse oocytes. *Genes Dev.* 24:2505–2516. https://doi.org/10.1101/gad.605910

Takeda, E., M. Hieda, J. Katahira, and Y. Yoneda. 2005. Phosphorylation of RanGAP1 stabilizes its interaction with ran and RanBP1. *Cell Struct. Funct.* 30:69–80. https://doi.org/10.1247/csf.30.69

Taltynov, O., J. Demeulemeester, F. Christ, S. De Houwer, V.G. Tsirkone, M. Gerard, S.D. Weeks, S.V. Strelkov, and Z. Debyser. 2013. Interaction of Transportin-SR2 with ras-related nuclear protein (Ran) GTPase. *J. Biol. Chem.* 288:25603–25613. https://doi.org/10.1074/jbc.M113.484345

Taus, T., T. Köcher, P. Pichler, C. Paschke, A. Schmidt, C. Henrich, and K. Mechtler. 2011. Universal and confident phosphorylation site localization using phosphoRS. *J. Proteome Res.* 10:5354–5362. https://doi.org/10.1021/pr200611n

Thawani, A., R.S. Kadzik, and S. Petry. 2018. XMAP215 is a microtubule nucleation factor that functions synergistically with the γ-tubulin ring complex. *Nat. Cell Biol.* 20:575–585. https://doi.org/10.1038/s41556-018-0091-6

Thomas, P.D., D. Ebert, A. Muruganujan, T. Mushayahama, L.-P. Albou, and H. Mi. 2022. Panther : Making genome-scale phylogenetics accessible to all. *Protein Sci.* 31:8–22. https://doi.org/10.1002/pro.4218

Tseng, B.S., L. Tan, T.M. Kapoor, and H. Funabiki. 2010. Dual detection of chromosomes and microtubules by the chromosomal passenger

complex drives spindle assembly. *Dev. Cell*. 18:903–912. https://doi.org/10.1016/j.devcel.2010.05.018

Tyanova, S., T. Temu, P. Sinitcyn, A. Carlson, M.Y. Hein, T. Geiger, M. Mann, and J. Cox. 2016. The perseus computational platform for comprehensive analysis of (prote)omics data. *Nat. Methods*. 13:731–740. https://doi.org/10.1038/nmeth.3901

Ustinova, K., F. Ruhnow, M. Gili, and T. Surrey. 2023. Microtubule binding of the human augmin complex is directly controlled by importins and Ran-GTP. *J. Cell Sci.* 136:jcs261096. https://doi.org/10.1242/jcs.261096

Van Itallie, E., M. Kalocsay, M. Wühr, L. Peshkin, and M.W. Kirschner. 2021. Transitions in the proteome and phospho-proteome during *Xenopus laevis* development. *bioRxiv*. https://doi.org/10.1101/2021.08.05.455309. (Preprint posted August 06, 2021).

Wang, B., M.J. Pfeiffer, H.C.A. Drexler, G. Fuellen, and M. Boiani. 2016. Proteomic analysis of mouse oocytes identifies PRMT7 as a reprogramming factor that replaces SOX2 in the induction of pluripotent stem cells. *J. Proteome Res.* 15:2407–2421. https://doi.org/10.1021/acs.jproteome.5b01083

Wiese, C., A. Wilde, M.S. Moore, S.A. Adam, A. Merdes, and Y. Zheng. 2001. Role of Importin-β in coupling ran to downstream targets in microtubule assembly. *Science*. 291:653–656. https://doi.org/10.1126/science.1057661

Wilbur, J.D., and R. Heald. 2013. Mitotic spindle scaling during *Xenopus* development by kif2a and importin α. *Elife*. 2:e00290. https://doi.org/10.7554/eLife.00290

Wilde, A., and Y. Zheng. 1999. Stimulation of microtubule aster formation and spindle assembly by the small GTPase ran. *Science*. 284:1359–1362. https://doi.org/10.1126/science.284.5418.1359

Wu, J., and A. Akhmanova. 2017. Microtubule-organizing centers. *Annu. Rev. Cell Dev. Biol.* 33:51–75. https://doi.org/10.1146/annurev-cellbio-100616-060615

Wühr, M., R.M. Freeman, M. Presler, M.E. Horb, L. Peshkin, S. Gygi, and M.W. Kirschner. 2014. Deep proteomics of the *Xenopus laevis* egg using an mRNA-Derived reference database. *Curr. Biol.* 24:1467–1475. https://doi.org/10.1016/j.cub.2014.05.044

Yamaguchi, R., and J. Newport. 2003. A role for Ran-GTP and Crm1 in blocking Re-Replication. *Cell*. 113:115–125. https://doi.org/10.1016/s0092-8674(03)00200-9

Yang, Y., L. Guo, L. Chen, B. Gong, D. Jia, and Q. Sun. 2023. Nuclear transport proteins: Structure, function, and disease relevance. *Signal Transduct. Target. Ther.* 8:425. https://doi.org/10.1038/s41392-023-01649-4

Zahn, N., C. James-Zorn, V.G. Ponferrada, D.S. Adams, J. Grzymkowski, D.R. Buchholz, N.M. Nascone-Yoder, M. Horb, S.A. Moody, P.D. Vize, et al. 2022. Normal table of *Xenopus* development: A new graphical resource. *Development*. 149:dev200356. https://doi.org/10.1242/dev.200356

Supplemental material

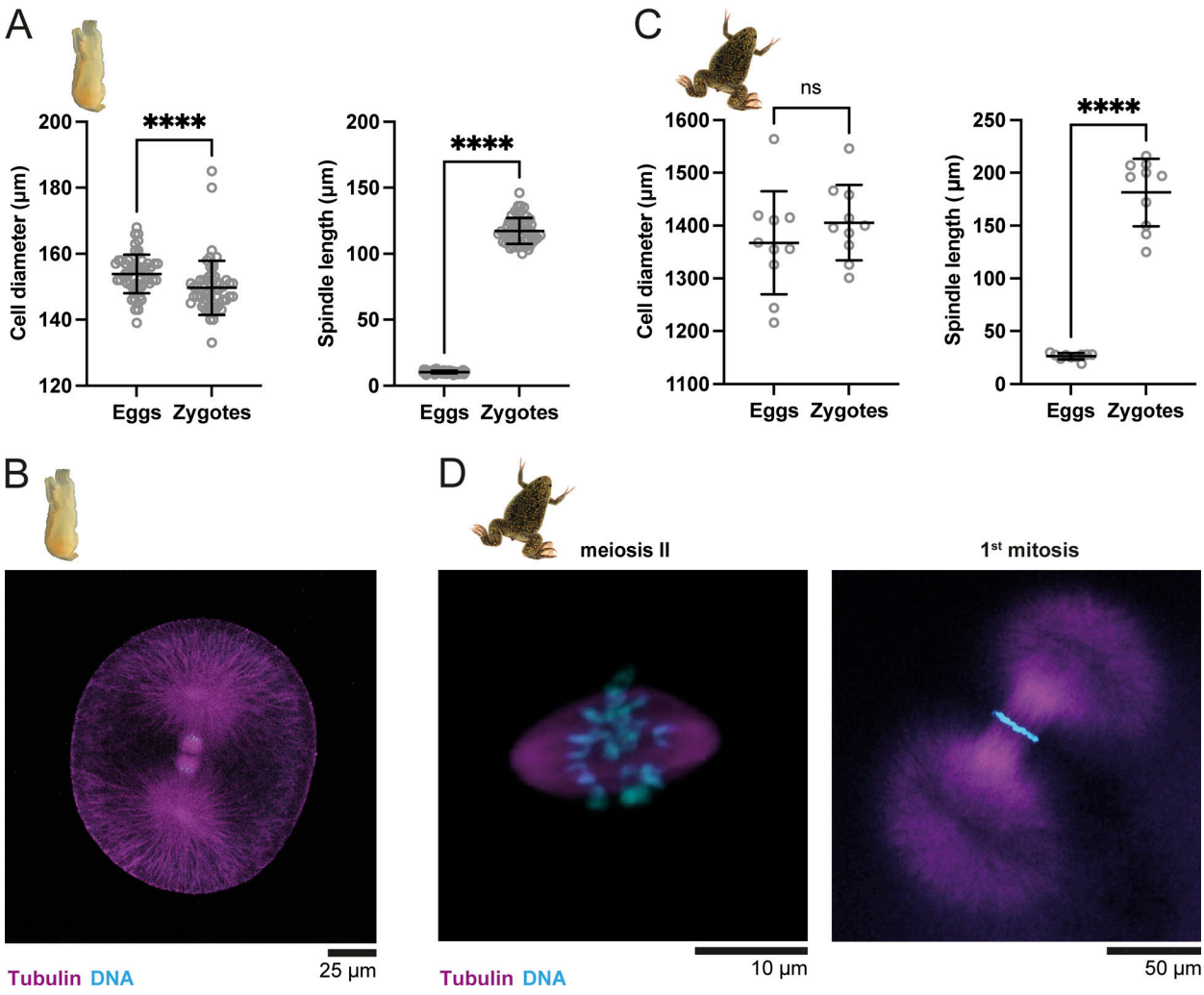

Figure S1. **Spindle length changes dramatically at the meiosis-to-mitosis transition in *Ciona* and *Xenopus*, though cell size does not. (A)** *C. robusta* cell diameter and metaphase spindle length (eggs $n = 58$, zygotes $n = 58$) measurements. Statistical significance was determined by two-tailed Mann–Whitney tests (**** = $P < 0.00005$). The line indicates the mean, and the error bars indicate one standard deviation above and below the mean. **(B)** Image of immunofluorescence of a representative *C. robusta* zygote in anaphase of the first mitosis. Tubulin (magenta), DNA (cyan). A single z-slice through the center of the spindle is shown. **(C)** *X. laevis* cell diameter and metaphase spindle length (eggs $n = 10$, zygotes $n = 10$) measurements. Statistical significance determined by two-tailed Mann–Whitney tests (ns = not significant, **** = $P < 0.00005$). The line indicates the mean and error bars indicate one standard deviation above and below the mean. **(D)** Higher magnification images of immunofluorescence of spindles from representative *X. laevis* eggs in metaphase of meiosis II (left panel) and zygotes in metaphase of the first mitosis (right panel) shown in Fig. 1 D. Tubulin (magenta), DNA (cyan). Maximum intensity projection is shown.

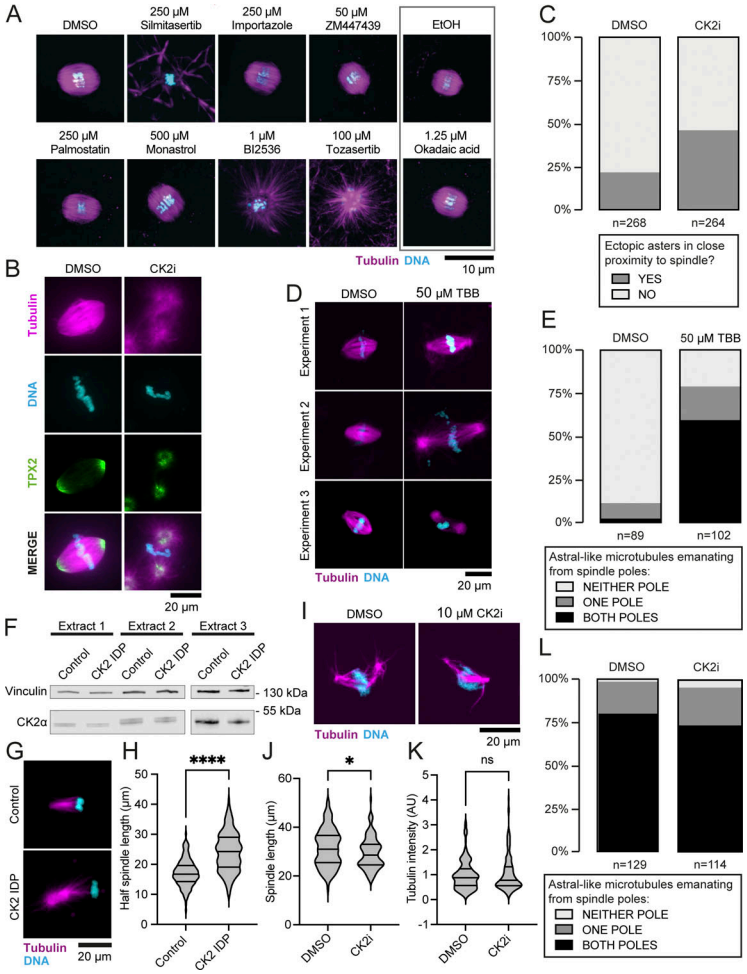

Figure S2. **Effects of small molecules on meiotic spindle morphology in *Ciona* oocytes and effects of CK2 inhibition on meiotic and mitotic *X. laevis* extracts. (A)** Images of immunofluorescence of representative *C. robusta* oocytes treated for 1 h with DMSO, 250 µM silmitasertib (CK2i), 250 µM RanGTP-importin β interaction inhibitor importazole, 250 µM APT1 inhibitor palmostatin, 500 µM Eg5 inhibitor monastrol, 1 µM Plk1 inhibitor BI2536, 50 µM Aurora A and B inhibitor ZM447439, 100 µM pan-aurora inhibitor tozasertib, EtOH, or 1.25 µM PP1 and PP2A inhibitor okadaic acid as indicated. Okadaic acid was in EtOH, and all other drugs were in DMSO. Maximum intensity projections are shown. Tubulin (magenta), DNA (cyan). DMSO control spindle image is the same as experiment 2 DMSO control spindle image in Fig. 2 A. **(B)** Images of immunofluorescence of representative spindles formed in metaphasic CSF *X. laevis* egg extract in the presence of 50 µM CK2i or DMSO as indicated. Maximum intensity projections are shown. Tubulin (magenta), DNA (cyan), mitotic spindle pole marker TPX2 (green). **(C)** Percentage of bipolar spindles displaying ectopic microtubule asters in proximity to the spindle in metaphasic CSF *X. laevis* egg extract in the presence of 50 µM CK2i or DMSO as indicated. Data from four independent extract experiments were pooled (n = 264 spindles [CK2i], n = 268 spindles [DMSO]); $n \geq 40$ spindles per condition for each extract. **(D)** Images of immunofluorescence of representative spindles formed in metaphasic CSF *X. laevis* egg extract in the presence of 50 µM TBB or DMSO as indicated for three independent experimental replicates. Maximum intensity projections are shown. Tubulin (magenta), DNA (cyan). **(E)** Percentage of bipolar spindles displaying astral-like microtubules emanating from both poles, one pole, or neither pole in metaphasic CSF *X. laevis* egg extract in the presence of 50 µM TBB or DMSO as indicated. Data from three independent extract experiments were pooled (n = 102 spindles [TBB], n = 89 spindles [DMSO]); $n \geq 13$ spindles per condition for each extract. **(F)** Western blots of CK2α and vinculin (loading control) in three *Xenopus* egg extracts following immunodepletion of CK2α using beads co-conjugated to CK2α and CK2β antibodies (CK2 IDP) or mock immunodepletion using beads conjugated to mouse IgG2 antibody (Control) as indicated. Estimated immunodepletion of 29% (extract 1), 30% (extract 2), and 26% (extract 3) of CK2α was achieved. **(G)** Representative images of half spindles from spindle assembly reactions carried out following immunodepletion of CK2α using beads co-conjugated to CK2α and CK2β antibodies (CK2 IDP) or mock immunodepletion using beads conjugated to mouse IgG2 antibody (Control) as indicated. β-tubulin (magenta), DNA (cyan). **(H)** Violin plot of half spindle length of half spindles from experiment described in G. $n \geq 169$ half spindles per condition (from three cytoplasmic extracts shown in F [$n \geq 48$ per extract for each condition]). **(I)** Images of immunofluorescence of representative spindles formed in metaphasic mitotic *X. laevis* embryo extract in the presence of 10 µM CK2i or DMSO as indicated. Maximum intensity projections are shown. Tubulin (magenta), DNA (cyan). **(J)** Violin plot of spindle length of spindles from spindle assembly reactions carried out in mitotic *Xenopus* embryo extract in the presence of DMSO or 10 µM CK2i as indicated. $n \geq 120$ spindles per condition (from three cytoplasmic extracts [$n \geq 23$ per condition per extract]). **(K)** Violin plot of β-tubulin intensity at spindle pole of spindles from spindle assembly reactions carried out in mitotic *X. laevis* embryo extracts in the presence of DMSO or 10 µM CK2i as indicated. n = 150 spindle poles per condition (from three cytoplasmic extracts [n = 50 per condition per extract]). Tubulin intensity normalized to mean of DMSO control. **(L)** Percentage of bipolar spindles displaying astral-like microtubules emanating from both poles, one pole, or neither pole in metaphasic mitotic *X. laevis* embryo extract in the presence of 10 µM CK2i or DMSO as indicated. Data from three independent extract experiments were pooled (n = 114 spindles [CK2i], n = 129 spindles [DMSO]); $n \geq 23$ spindles per condition for each extract. Statistical significance was determined by two-tailed Mann–Whitney tests (**** = $P < 0.00005$, * = $P < 0.05$, ns = not significant). For violin plots, lines indicate the median and upper and lower quartiles. Source data are available for this figure: SourceData FS2.

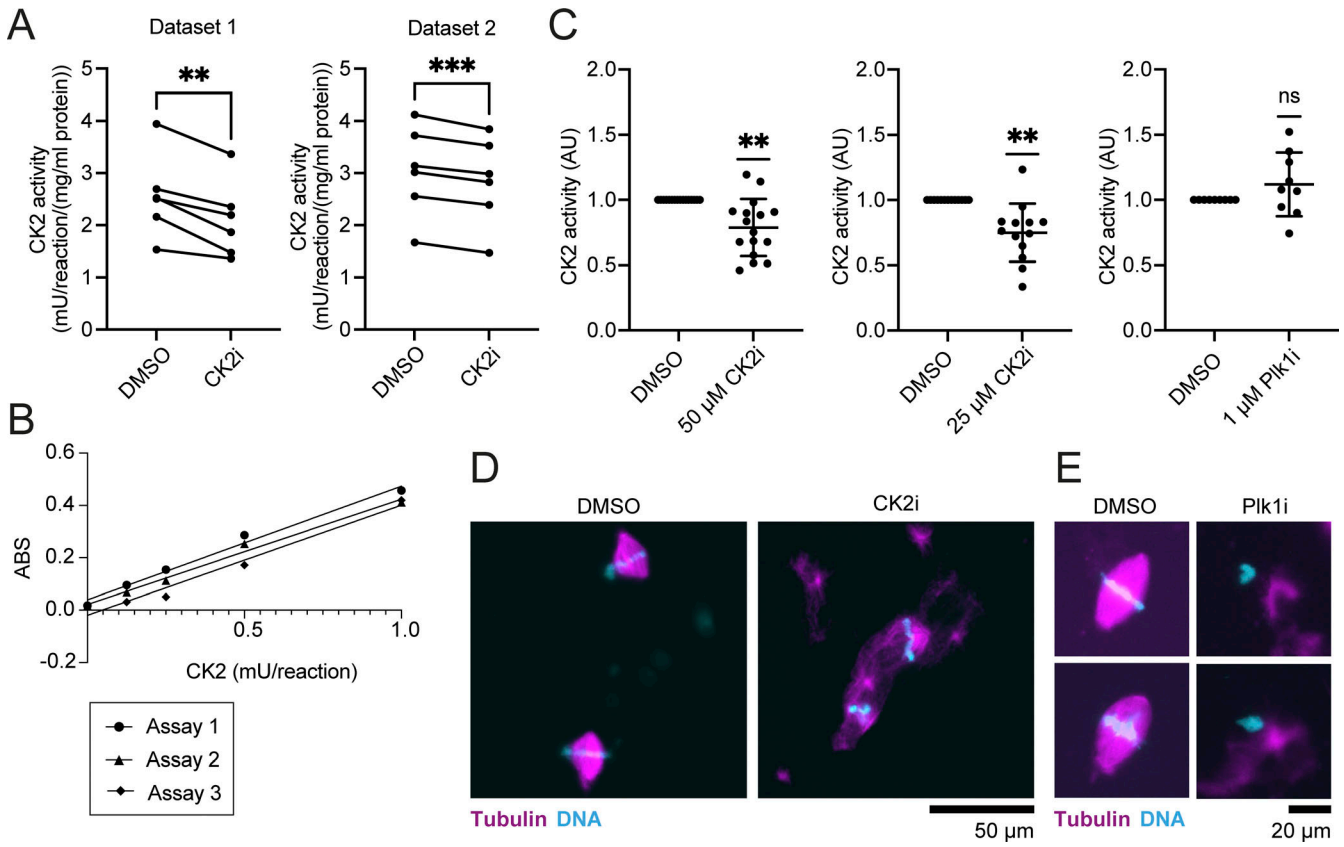

Figure S3. **CK2 activity is reduced by CK2 inhibition in *X. laevis* extract. (A)** CK2 activity of six extracts (three meiotic and three mitotic) used in proteomics and phosphoproteomics experiments in control and CK2i treated samples for each dataset. Statistical significance was determined by paired two-tailed *t* tests (** = P < 0.005, *** = P < 0.0005). Data distribution was assumed to be normal, but this was not formally tested. **(B)** Results of CK2 activity assay of samples containing 0–1 mU/reaction of purified CK2 alpha/beta protein (MBL) three times on different days (assays 1, 2, and 3). Linear regression analysis was used to fit a trendline to absorbance data from each assay. The slopes of the trendlines of the three assays were not significantly different (P = 0.7962). **(C)** CK2 activity of 500 μg/ml meiotic *Xenopus* egg extracts treated with 50 μM CK2i (*n* = 16 extracts), 25 μM CK2i (*n* = 13 extracts), or 1 μM Plk1i (*n* = 9 extracts) normalized to DMSO control. Statistical significance was determined by one sample two-tailed *t* test against hypothetical mean of 1 (** = P < 0.005). Data distribution was assumed to be normal, but this was not formally tested. **(D)** Images of immunofluorescence of representative fields of metaphasic CSF *X. laevis* egg extract spindle assembly reactions in the presence of 25 μM CK2i or DMSO as indicated. Maximum intensity projections are shown. Tubulin (magenta), DNA (cyan). **(E)** Images of immunofluorescence of representative fields of metaphasic CSF *X. laevis* egg extract spindle assembly reactions in the presence of 1 μM Plk1i or DMSO as indicated. Maximum intensity projections are shown. Tubulin (magenta), DNA (cyan).

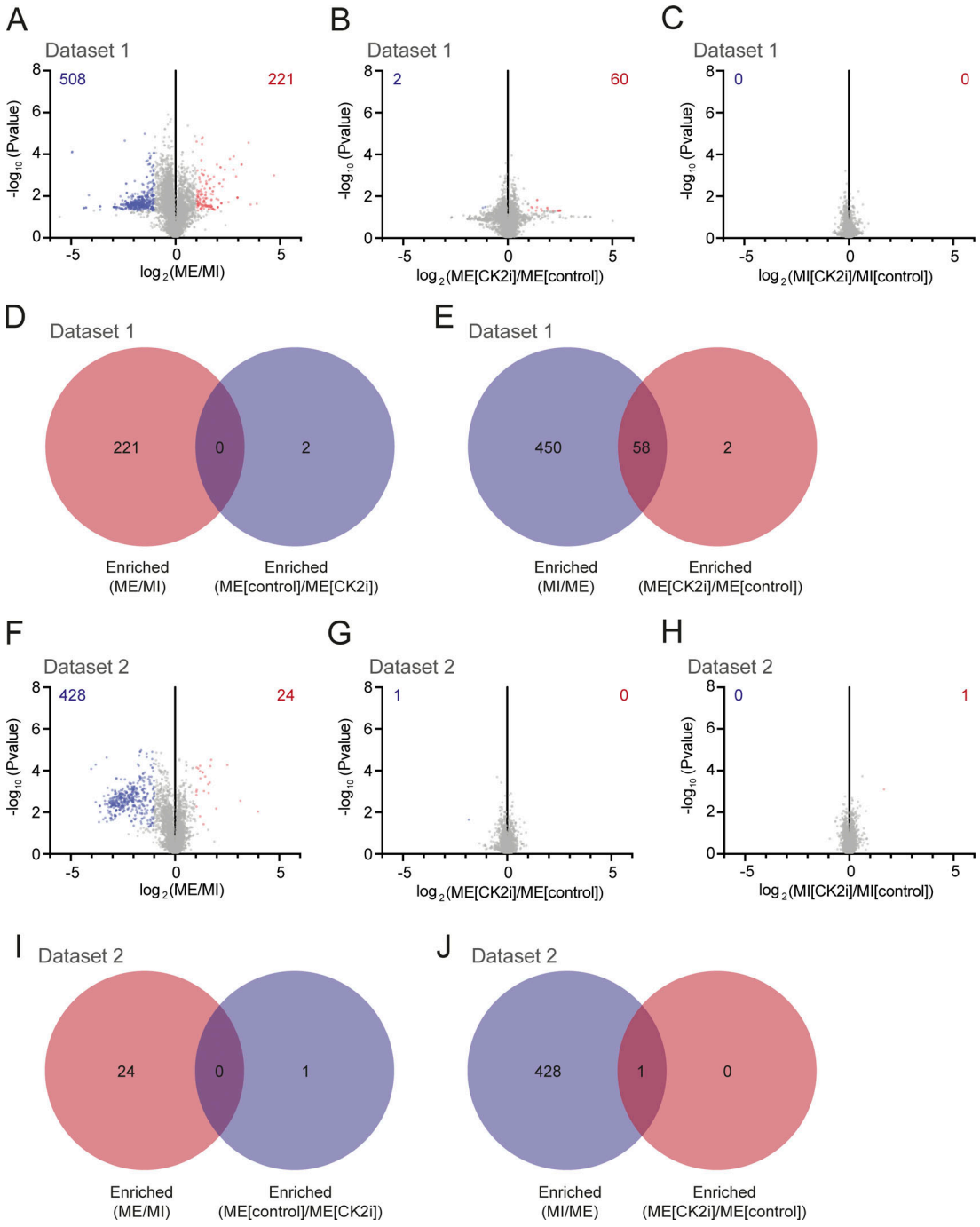

Figure S4. **Proteomic changes between meiosis and mitosis and upon CK2 inhibition. (A–C)** Volcano plots of dataset 1 $\log_2$ ratio (protein abundance) versus $-\log_{10}$ P value for individual proteins in meiosis compared to mitosis (ME/MI) (A), meiosis in the presence of CK2i compared to meiosis in the absence of CK2i (B), and mitosis in the presence of CK2i compared to mitosis in the absence of CK2i (C), respectively. Red points indicate significantly enriched ($\log_2$ ratio >1 and P value <0.05) proteins (total number indicated in red). Blue points indicate significantly depleted ($\log_2$ ratio less than −1 and P value <0.05) proteins (total number indicated in blue). *n* = 8,157 proteins. **(D)** Venn diagram indicating the number of unique proteins in dataset 1 in the categories enriched in meiosis relative to mitosis and enriched in meiosis in the absence of CK2i relative to meiosis in the presence of CK2i and in the overlap between these two categories. **(E)** Venn diagram indicating the number of unique proteins in dataset 1 in the categories enriched in mitosis relative to meiosis and enriched in meiosis in the presence of CK2i relative to meiosis in the absence of CK2i and in the overlap between these two categories. **(F–H)** Volcano plots of dataset 2 $\log_2$ ratio (protein abundance) versus $-\log_{10}$ P value for individual proteins in meiosis compared to mitosis (ME/MI) (F), meiosis in the presence of CK2i compared to meiosis in the absence of CK2i (G), and mitosis in the presence of CK2i compared to mitosis in the absence of CK2i (H), respectively. Red points indicate significantly enriched ($\log_2$ ratio >1 and P value <0.05) proteins (total number indicated in red). Blue points indicate significantly depleted ($\log_2$ ratio less than −1 and P value <0.05) proteins (total number indicated in blue). *n* = 7,948 proteins. **(I)** Venn diagram indicating the number of unique proteins in dataset 2 in the categories enriched in meiosis relative to mitosis and enriched in meiosis in the absence of CK2i relative to meiosis in the presence of CK2i and in the overlap between these two categories. **(J)** Venn diagram indicating the number of unique proteins in dataset 2 in the categories enriched in mitosis relative to meiosis and enriched in meiosis in the presence of CK2i relative to meiosis in the absence of CK2i and in the overlap between these two categories.

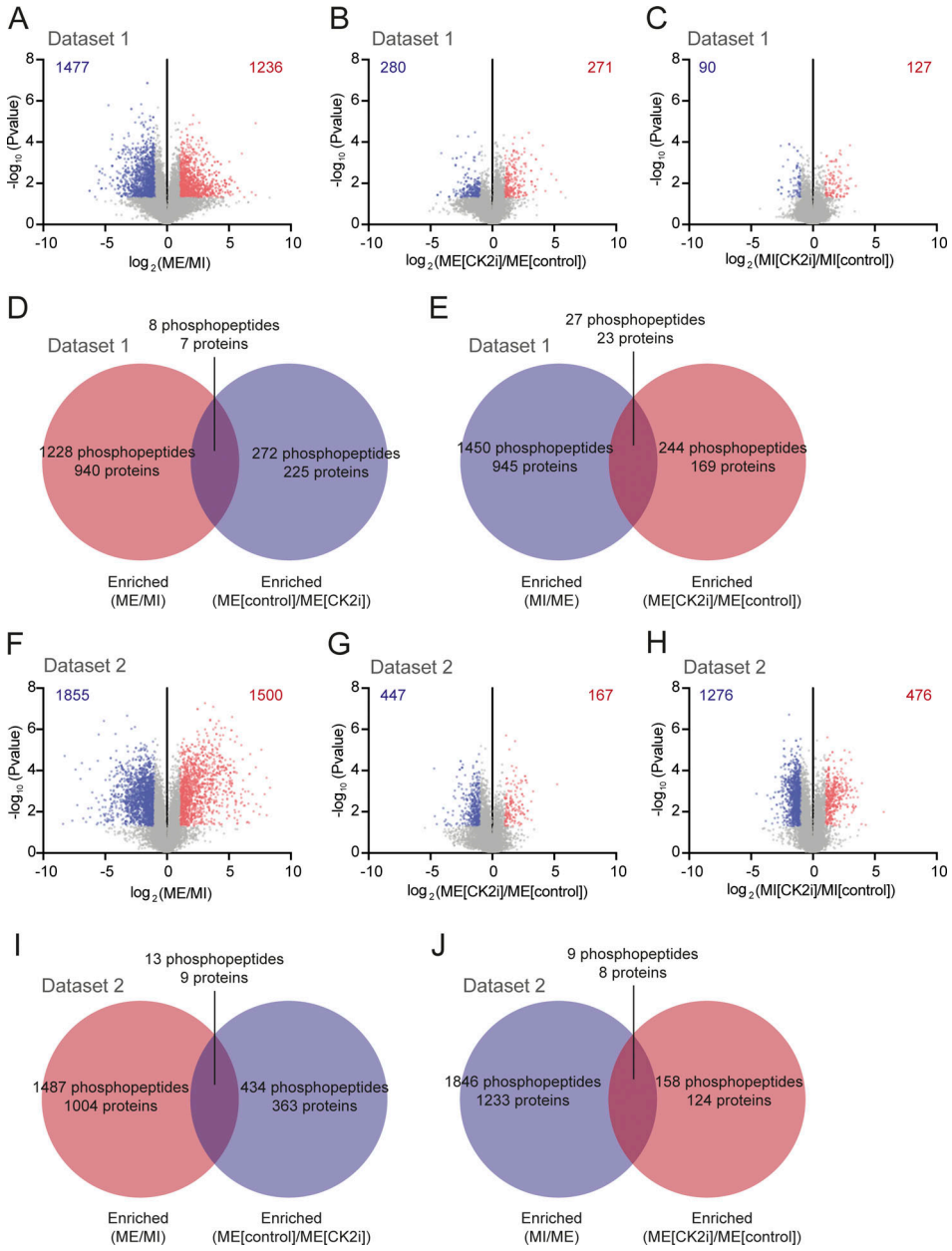

Figure S5. **Phosphoproteomic changes between meiosis and mitosis and upon CK2 inhibition. (A–C)** Volcano plots of dataset 1 $\log_2$ ratio (phosphopeptide abundance) versus $-\log_{10}$ P value for individual phosphopeptides in meiosis compared to mitosis (ME/MI) (n = 14,721 phosphopeptides) (A), meiosis in the presence of CK2i compared to meiosis in the absence of CK2i (n = 14,721 phosphopeptides) (B), and mitosis in the presence of CK2i compared to mitosis in the absence of CK2i (n = 14,721 phosphopeptides) (C), respectively. Red points indicate significantly enriched ($\log_2$ ratio >1 and P value <0.05) phosphopeptides (total number indicated in red). Blue points indicate significantly depleted ($\log_2$ ratio less than −1 and P value <0.05) phosphopeptides (total number indicated in blue). **(D)** Venn diagram indicating the number of unique phosphopeptides and proteins containing phosphopeptides in dataset 1 in the categories enriched in meiosis relative to mitosis and enriched in meiosis in the absence of CK2i relative to meiosis in the presence of CK2i and in the overlap between these two categories that do not exhibit protein-level changes in the same directions. **(E)** Venn diagram indicating the number of unique phosphopepetides and proteins containing phosphopeptides in dataset 1 in the categories enriched in mitosis relative to meiosis and enriched in meiosis in the presence of CK2i relative to meiosis in the absence of CK2i and in the overlap between these two categories that do not exhibit protein-level changes in the same directions. **(F–H)** Volcano plots of dataset 2 $\log_2$ ratio (phosphopeptide abundance) versus $-\log_{10}$ P value for individual phosphopeptides in meiosis compared to mitosis (ME/MI) (n = 13,892 phosphopeptides) (F), meiosis in the presence of CK2i compared to meiosis in the absence of CK2i (n = 13,863 phosphopeptides) (G), and mitosis in the presence of CK2i compared to mitosis in the absence of CK2i (n = 13,877 phosphopeptides), (H) respectively. Red points indicate significantly enriched ($\log_2$ ratio >1 and P value <0.05) phosphopeptides (total number indicated in red). Blue points indicate significantly depleted ($\log_2$ ratio less than −1 and P value <0.05) phosphopeptides (total number indicated in blue). n = 13,892 phosphopeptides. **(I)** Venn diagram indicating the number of unique phosphopeptides and proteins containing phosphopeptides in dataset 2 in the categories enriched in meiosis relative to mitosis and enriched in meiosis in the absence of CK2i relative to meiosis in the presence of CK2i and in the overlap between these two categories that do not exhibit protein-level changes in the same directions. **(J)** Venn diagram indicating the number of unique phosphopepetides and proteins containing phosphopeptides in dataset 2 in the categories enriched in mitosis relative to meiosis and enriched in meiosis in the presence of CK2i relative to meiosis in the absence of CK2i and in the overlap between these two categories that do not exhibit protein-level changes in the same directions.

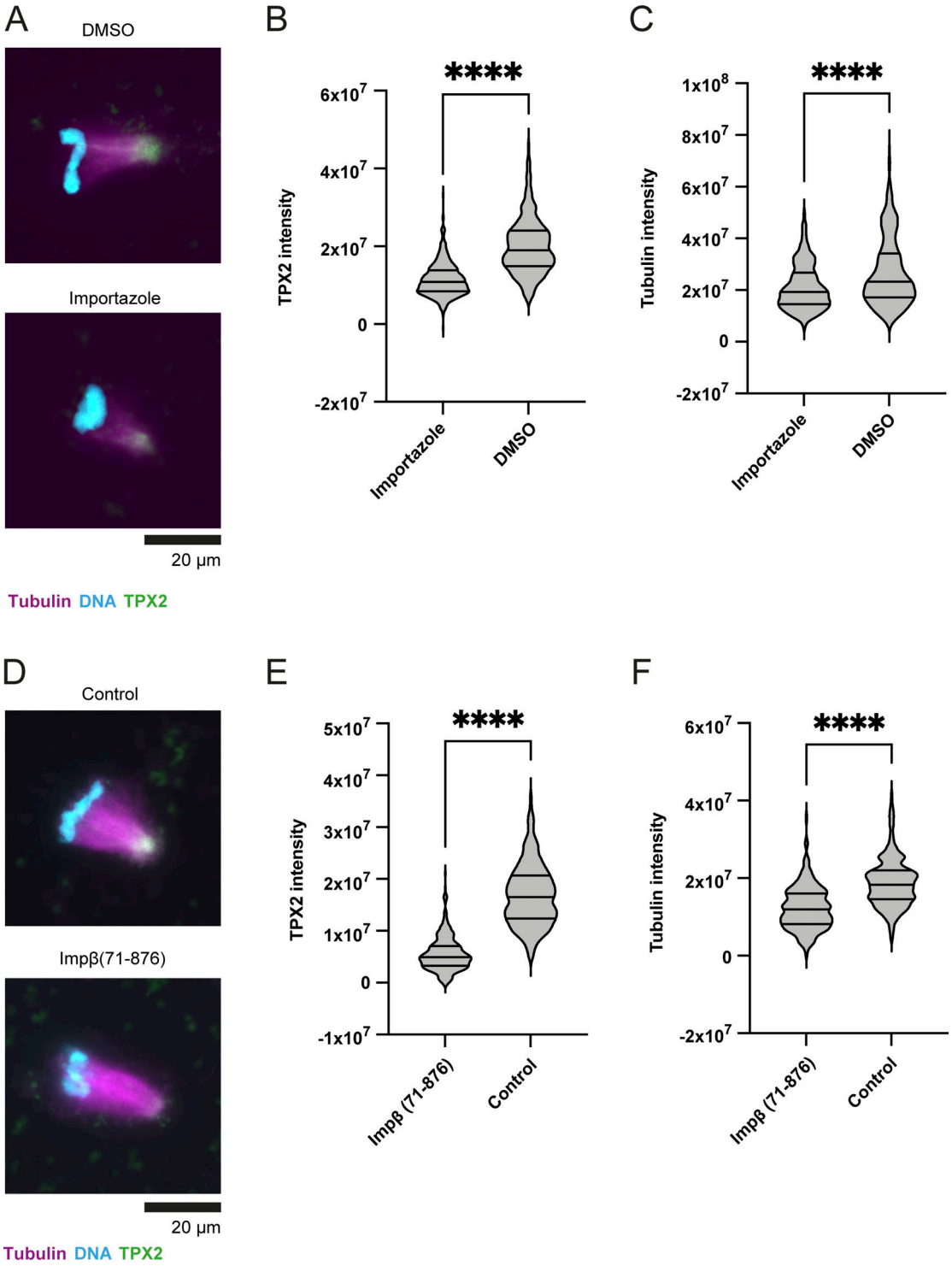

Figure S6. **Inhibition of RanGTP-mediated spindle assembly pathway reduces TPX2 and tubulin intensity at spindle poles in *X. laevis* egg extracts. (A)** Representative images of half spindles from spindle assembly reactions carried out in the presence of DMSO or 300 µM importazole as indicated. β-tubulin (magenta), DNA (cyan), and TPX2 (green). DMSO and importazole spindle images are the same as DMSO and importazole spindle images in Fig. 5 C with different display settings to allow visualization of TPX2. **(B and C)** Violin plots of TPX2 intensity (B) or β-tubulin intensity (C) of half spindles from experiment described in (A). $n \geq 420$ half spindles per condition (from three cytoplasmic extracts [$n \geq 133$ per extract for each condition]). **(D)** Representative images of half spindles from spindle assembly reactions carried out in the presence of XB (control) or 2.5 µM importin-β(71–876) as indicated. β-tubulin (magenta), DNA (cyan), and TPX2 (green). DMSO spindle image is the same as DMSO spindle image in Fig. 5 D with different display settings to allow visualization of TPX2. **(E and F)** Violin plot of TPX2 intensity (E) or β-tubulin intensity (F) of half spindles from experiment described in B. $n \geq 329$ half spindles per condition (from three cytoplasmic extracts [$n \geq 92$ per extract for each condition]). Statistical significance was determined by two-tailed Mann–Whitney tests (**** = $P < 0.00005$). The lines indicate the median and upper and lower quartiles. Data are a subset of data plotted in Fig. 5.

Provided online are Table S1, Table S2, Table S3, Table S4, Table S5, Table S6, Table S7, and Table S8. Table S1 shows the summary of proteomic data. Table S2 shows the summary of phosphoproteomic data. Table S3 shows the GO enrichment analysis results—proteins enriched in meiosis relative to mitosis. Table S4 shows the microtubule-binding proteins enriched in meiosis relative to mitosis. Table S5 shows the GO enrichment analysis results—proteins enriched in mitosis relative to meiosis. Table S6 shows the GO enrichment analysis results—proteins with phosphosites enriched in mitosis. Table S7 shows the proteins in spindle GO category (GO:0005819) with phosphosites enriched in mitosis relative to meiosis. Table S8 shows the candidate proteins annotated with localization data.